1    Input-specific synaptic depression shapes temporal integration in mouse visual cortex
2
3                           Jennifer Y. Li and Lindsey L. Glickfeld
4        Department of Neurobiology, Duke University Medical Center, Durham, NC 27701, USA
5
6    Abbreviated title: Synaptic depression drives rapid adaptation
7    Page Count: 24
8    Figure Count: 8 main + 8 supplemental
9    Word count:
10           Summary- 145
11           Introduction- 647
12           Results- 3657
13           Discussion- 1456
14
15   Keywords: adaptation, stimulus-specific suppression, paired-pulse plasticity, vesicle depletion,
16   intracellular electrophysiology, extracellular electrophysiology, layer 4, layer 2/3, pyramidal cell,
17   excitation, inhibition
18
19   Proofs and correspondence to:
20   glickfeld@neuro.duke.edu

**Summary**

Efficient sensory processing requires the nervous system to adjust to ongoing features of the environment. In primary visual cortex (V1), neuronal activity strongly depends on recent stimulus history. Existing models can explain effects of prolonged stimulus presentation, but remain insufficient for explaining effects observed after shorter durations commonly encountered under natural conditions. We investigated the mechanisms driving adaptation in response to brief (100 ms) stimuli in L2/3 V1 neurons by performing *in vivo* whole-cell recordings to measure membrane potential and synaptic inputs. We find that rapid adaptation is generated by stimulus-specific suppression of excitatory and inhibitory synaptic inputs. Targeted optogenetic experiments reveal that these synaptic effects are due to input-specific short-term depression of transmission between layers 4 and 2/3. Thus, distinct mechanisms are engaged following brief and prolonged stimulus presentation and together enable flexible control of sensory encoding across a wide range of time scales.

**Introduction**

Adaptation plays a key role in dynamic regulation of sensory systems. A proposed function of sensory adaptation is to maximize stimulus information from the environment while minimizing metabolic cost of the nervous system, also known as the efficient coding hypothesis[1–3]. This optimization is particularly important in the context of naturalistic stimuli, which contain highly correlated temporal and spatial structure[4–6]. By reducing neuronal sensitivity to repeated or relatively constant stimulus features, adaptation can improve the metabolic efficiency of stimulus representation. To accomplish this, sensory systems must account for the redundancy of current stimulus features by referencing a stored memory of stimulus statistics and modulate responses accordingly.

Notably, naturalistic stimuli fluctuate over a wide range of timescales, spanning milliseconds to many minutes, and these dynamics are further enriched by self-generated movements during active sensation[7,8]. Therefore, reducing redundant encoding across timescales requires sensory systems to concurrently store stimulus statistics across a wide range of temporal contexts. Indeed, measured effects of adaptation can accrue over a variety of timescales. Responses recorded from neurons in visual, auditory, and somatosensory cortices are best predicted by sets of temporal filters that encompass multiple timescales of stimulus history[9,10]. However, whether adaptation acts to improve encoding through a singular mechanism that acts on multiple timescales, or multiple mechanisms, is still unknown.

Part of this ambiguity arises from the complexity of biological processes related to adaptation. Ion channel kinetics and short-term synaptic plasticity can often be fit with concurrent fast and slow time constants that differ by orders of magnitude[1,11–14]. However, studies that have systematically measured adaptation across multiple timescales provide strong evidence for contribution from multiple, distinct mechanisms. In the retina, fast and slow contrast adaptation modulate retinal circuitry in different ways[15]. At the level of primary visual cortex (V1), brief and prolonged presentation of the same visual stimulus produce distinct effects on neurons' orientation tuning curves[16]. This idea extends even to human psychophysics, where duration and dynamics of adapter stimuli can determine not only the magnitude, but also specific features of perceived visual aftereffects[17,18]. Altogether, both perceptual and neural effects of adaptation are consistent with multiple mechanisms that act across different timescales.

Here, we investigated the mechanism underlying adaptation in layer 2/3 (L2/3) neurons in V1 of alert mice. L2/3 neurons in V1 undergo a profound degree of adaptation to brief stimulus presentations (0.1 s; rapid adaptation)[19,20]. Consistent with an efficient coding model, visual responses to repeated stimuli are suppressed more than responses to novel stimuli. Although adaptation could be inherited through many stages of visual processing prior to L2/3, the majority of this effect appears to originate within cortex, as neurons in both the visual thalamus (lateral geniculate nucleus; LGN) and the thalamic input layer of cortex (layer 4; L4) show very little effect of adaptation at this time scale[20,21]. Although cell-intrinsic mechanisms can explain adaptation effects with prolonged stimulus presentation[22,23], they are insufficient for explaining rapid adaptation's relatively brief time scale of induction as well as stimulus-selectivity. Instead, these features have largely been attributed to mechanisms involving inhibition and short-term synaptic plasticity[14,24–28]. However, the mechanisms engaged with rapid adaptation have yet to be directly tested.

Using a combination of *in vivo* and *in vitro* electrophysiological approaches, we measured the relative contribution of cell-intrinsic and synaptic mechanisms to this form of rapid adaptation. We find that adaptation with brief visual stimulus presentation does not engage significant hyperpolarization mechanisms. Instead, we find balanced a decrease in both excitatory and inhibitory synaptic inputs that can account for the decreasing in firing rate associated with rapid adaptation. Manipulations that directly

77  activate L4, or decrease probability of release at L4 synapses, demonstrate that this site is both
78  necessary and sufficient for rapid adaptation, and argue for a role of short-term depression at this
79  synapse. Altogether, our results highlight a complementary role for cell-intrinsic and synaptic
80  mechanisms in maintaining multiple time scales of sensory adaptation.
81
82  **Results**
83  *Rapid adaptation reduces stimulus-evoked synaptic inputs*
84  Visual responses of neurons in L2/3 of V1 are substantially reduced following even brief (0.1 s)
85  visual stimuli[9,19,21]. This is largely a cortical phenomenon as neurons in the thalamic input layer of V1 (L4)
86  undergo significantly less suppression than those in L2/3[20]. Thus, this rapid adaptation is likely due to a
87  local mechanism affecting cell-intrinsic excitability of L2/3 neurons or the efficacy of their synaptic inputs.
88  Previous work investigating cortical mechanisms of adaptation revealed that extended visual stimulus
89  presentation (tens of seconds) evokes a cell-intrinsic hyperpolarization that accounts for decreased
90  stimulus-evoked responses[22,23]. We first investigated whether rapid adaptation is also mediated by cell-
91  intrinsic mechanisms by making intracellular membrane potential recordings of L2/3 V1 neurons in
92  awake, head-fixed mice. Pairs of high-contrast, static gratings (0.1 s, 0.1 cycles per degree, 30° diameter)
93  at the neuron's preferred orientation were presented at a range of inter-stimulus intervals (ISIs) to
94  measure the magnitude and time course of recovery from rapid adaptation (**Figure 1A**). Presentation of
95  the baseline stimulus induces a decrease in firing rate (FR) in response to the test that is consistent with
96  previous studies using calcium imaging and extracellular recordings[19,20] (**Figure 1B**). At short ISIs,
97  responses to the test stimulus are suppressed by nearly 40% (normalized FR [0.25 s ISI]: 0.62 ± 0.08; n
98  = 13 cells; $p < 0.001$, paired t-test; **Figure 1C**) and recover with a time constant of nearly 1 second ($\tau$ =
99  0.82 s).
100  To determine whether this decrease in firing rate could be explained by a long-lasting
101  hyperpolarization following the baseline stimulus, we compared the membrane potential preceding
102  baseline and test stimuli. Despite the strong suppression of spike output, there is no significant
103  hyperpolarization of membrane potential prior to the test stimulus (0.25 s ISI – baseline: -58.72 ± 2.25
104  mV; test: -58.25 ± 2.50 mV; $p = 0.74$, paired t-test; **Figure 1D**). Other properties of the recorded cell that
105  could impact spike output are also unchanged, such as the spike threshold (0.25 s ISI – baseline: -40.07
106  ± 1.01 mV; test: -40.32 ± 1.15 mV; $p = 0.50$, paired t-test; **Figure 1E**) and membrane variance (0.25 s ISI
107  – baseline: 7.63 ± 1.88 mV$^2$; test: 7.54 ± 1.94 mV$^2$; $p = 0.85$, paired t-test; **Figure 1F**). Additionally, most
108  neurons have a positive correlation between the number of spikes in response to baseline and test stimuli
109  on each trial, arguing against a cell-intrinsic fatigue effect (**Figure S1A**). Although a cell-intrinsic
110  hyperpolarization mechanism exists in V1 L2/3 neurons, these changes in membrane potential appear
111  only after prolonged periods of activity (**Figure S1B-D**). Instead, adaptation in response to brief stimuli
112  greatly reduces stimulus-evoked post-synaptic potentials (PSPs), with a similar magnitude (normalized
113  PSP [0.25 s ISI]: 0.51 ± 0.11; **Figure 1B-C, G**) and time course of recovery ($\tau$ = 0.79 s) as is seen for
114  changes in spike output. Therefore, rapid adaptation engages a synaptic, rather than cell-intrinsic,
115  mechanism to reduce stimulus-evoked responses to repeated stimuli.
116  Stimulus-evoked PSPs are generated by the sum of both excitatory and inhibitory inputs onto a
117  post-synaptic cell. Increases in inhibition, decreases in excitation, or decreases in total conductance
118  could all lead to reduced stimulus-evoked depolarization. To identify changes in stimulus-evoked
119  excitation and inhibition, we made voltage clamp recordings from L2/3 neurons while presenting the same
120  stimulus paradigm (**Figure 2A**). We recorded both excitatory currents (EPSCs) and inhibitory currents

121 (IPSCs) from individual neurons by clamping the membrane potential near the reversal for inhibition (-70
122 mV) and excitation (+10 mV), respectively (n = 10 cells; **Figure 2A** and **S2A**). Consistent with our current
123 clamp recordings, there are no changes in either the mean or the standard deviation of the holding current
124 in the time windows preceding baseline and test stimulus onset (-70 mV: Δ current -2.33 ± 12.21 pA; p =
125 0.86; Δ std 0.67 ± 3.65 pA; p = 0.44; +10 mV: Δ current -2.79 ± 15.90 pA; p = 0.86, Δ std -4.14 ± 6.07 pA;
126 p = 0.28; paired t-test for all comparisons). This argues against a role for long-lasting inhibition or changes
127 in overall network excitability in rapid adaptation.
128        Instead, there is a robust decrease in the peak amplitude of stimulus-evoked excitation
129 (normalized EPSC: 0.51 ± 0.06; p < 0.001, paired t-test; **Figure 2B-C**) and inhibition (normalized IPSC:
130 0.47 ± 0.09; p < 0.001, paired t-test) in response to the test stimulus relative to baseline. This reduces
131 the overall conductance (baseline: 7.45 ± 3.11 nS; test: 3.87 ± 2.76 nS; p < 0.001, paired t-test) while
132 preserving E/I ratio (baseline: 0.81 ± 0.16; test: 0.95 ± 0.27; p = 0.16, paired t-test; **Figure 2D**). Stimulus-
133 evoked synaptic inputs are suppressed to a similar degree as the postsynaptic potentials (EPSC vs PSP:
134 p = 0.98; IPSC vs PSP: p = 0.94; unpaired t-test) and firing rates (EPSC vs FR: p = 0.19; IPSC vs FR: p
135 = 0.16; unpaired t-test) measured intracellularly, and recover at a similar time scale ($\tau_{EPSC}$ = 1.10 s; $\tau_{IPSC}$
136 = 0.93 s; **Figure 2C**). Thus, the decrease in synaptic drive can account for the magnitude and time course
137 of the reduced excitability following rapid adaptation.
138        Notably, the magnitude and time course of changes in excitatory and inhibitory synaptic inputs
139 are remarkably well-matched (**Figure 2C-D**). This suggests that the two may be yoked by a shared
140 mechanism, such as a decrease in the excitation onto both excitatory and inhibitory cells. Indeed, we find
141 a comparable decrease in the firing rate of both putative excitatory (regular-spiking [RS], n = 135 units)
142 and inhibitory (fast-spiking [FS], n = 67 units) neurons in L2/3 (normalized FR [0.25 s ISI]: RS = 0.65 ±
143 0.02, FS = 0.71 ± 0.04, p = 0.08, unpaired t-test; **Figures 2E and S3A-B**). Altogether, these observations
144 are consistent with short-term depression of excitatory synapses onto both excitatory and inhibitory
145 neurons.
146
147 *Adaptation acts at specific excitatory synapses*
148        If reduction in excitation and inhibition in L2/3 neurons *in vivo* is generated by short-term synaptic
149 depression of intracortical synapses, changes in synaptic inputs should reflect the features of this type of
150 plasticity. First, we expect that repeated visual stimulus presentations will drive increasing depression of
151 visual responses and eventually saturate at a level determined by the balance between time constants
152 of vesicle depletion and replenishment[11,12,14]. Second, these effects should be restricted to the specific
153 subset of synapses activated by features of the baseline stimulus (**Figure 3A**). To test these predictions,
154 we measured EPSCs and IPSCs in response to static gratings of matched and orthogonal orientations
155 (0.1 s duration each). We presented five stimuli of the same orientation (baseline and test 1-4) to measure
156 accumulation/saturation, followed by an orthogonal grating to measure specificity (test 5).
157        Our results confirm both predictions. First, we find that suppression of both EPSCs and IPSCs
158 accumulate and saturate over the five repeated stimuli (n = 8 cells; test 1 vs baseline 1, p = 0.04 for
159 EPSCs and p = 0.009 for IPSCs; test 2-4 vs baseline, p < 0.001 for EPSCs and IPSCs; all comparisons
160 within test 2-4, p > 0.05 for EPSCS and IPSCS; one-way ANOVA with post hoc Tukey test; **Figure 3B**).
161 Second, excitation and inhibition evoked by the fifth, orthogonal test stimulus are not significantly different
162 from the baseline response at that orientation (test 5 vs baseline: EPSCs p = 0.89; IPSCs p = 0.98; paired
163 t-test), consistent with a synapse-specific mechanism.

164  Across all stimuli presented, excitation and inhibition remain balanced relative to baseline levels
165  (p = 0.81; effect of current type, two-way ANOVA), which we attribute to a parallel decrease in excitatory
166  drive to pyramidal cells and interneurons. We further tested this by probing the orientation selectivity of
167  adaptation of excitation and inhibition. If decreases in EPSCs and IPSCs are the result of short-term
168  depression at excitatory synapses, the orientation selectivity of adaptation of excitation and inhibition
169  should be matched. Additionally, this selectivity should reflect the tuning of spike output in pyramidal
170  neurons, which are generally more narrowly tuned than interneurons[29–31]. To measure the tuning width
171  of adaptation, we measured excitation and inhibition in response to pairs of stimuli with orientation
172  differences between 0 and 90 degrees, sampled in 22.5 degree increments (0.25 s ISI only; **Figure 3C**).
173  We find that the degree of adaptation depends on orientation difference (n = 13 cells; two-way ANOVA:
174  main effect of orientation, p = 0.009) but not current type. EPSCs and IPSCs undergo a similar degree
175  of suppression across all orientation differences (main effect of current type: p = 0.32).
176  To determine whether the orientation selectivity of this suppression matches the orientation tuning
177  of spike output in V1 neurons, we fit individual neurons' normalized EPSCs and IPSCs in response to the
178  test stimulus with a von Mises function (**Figure 3D**). We then compared these intracellular adaptation
179  tuning curves to the orientation tuning curves of either RS or FS units obtained in extracellular recordings
180  (**Figure 3E** and **S3C**). We find that the bandwidth of adaptation observed in EPSCs and IPSCs more
181  closely matches the bandwidth of orientation tuning of RS units than FS units (tuning width (TW): RS =
182  21.31 ± 1.25, FS = 26.78 ± 1.91; EPSC = 19.15 ± 3.36, IPSC = 21.57 ± 3.44). The match between the
183  orientation-selectivity of adaptation of IPSCs and RS tuning further supports the idea that changes in
184  excitation and inhibition are yoked by a shared short-term depression mechanism that reduces excitation
185  onto both classes of L2/3 neurons.
186
187  *Activation of L4 depresses excitatory inputs in L2/3*
188  Our data suggest that rapid adaptation is due to short-term depression of excitatory synapses in
189  L2/3. If so, direct activation of synaptic inputs onto L2/3 neurons should induce short-term depression
190  and be sufficient to mimic the effects of visual adaptation. To test this prediction, we optogenetically
191  activated inputs to L2/3 *in vitro* in slices from mice expressing Channelrhodopsin-2 (ChR2) selectively in
192  L4 pyramidal neurons (Scnn1a-Tg3-Cre x Ai32 mice) by targeting the blue excitation light to L4 below
193  the recorded cell (**Figure 4A**; **STAR Methods**). Optogenetic activation of cells in L4 for 0.1 s activates
194  monosynaptic and polysynaptic excitatory inputs to L2/3 neurons (**Figure 4B**). Repeated stimulation of
195  L4 (baseline and test), reveals a history-dependent reduction of these optogenetically-evoked EPSCs.
196  As with the *in vivo* recordings, at short ISIs responses to the test stimulus are suppressed by nearly 40%
197  (normalized EPSC amplitude [0.25 s ISI]: 0.63 ± 0.01; n = 11 cells; p <0.001, paired t-test; **Figure 4C**)
198  and responses recover with a time constant of nearly 1 second ($\tau$ = 1.03 s). Therefore, the long-lasting
199  suppression of excitatory input to L2/3 neurons observed with rapid adaptation *in vivo* can be reproduced
200  by engaging a local, activity-dependent mechanism in V1.
201  In the context of the local V1 circuit, L4 stimulation *in vitro* could drive short-term depression at
202  L4 to L2/3 synapses or at L2/3 to L2/3 synapses. To determine whether these synapses depress equally
203  or in an input-specific manner[32,33], we used electrical stimulation to selectively drive monosynaptic inputs
204  from L4 or L2/3 onto L2/3 neurons (**Figure 4D**; **STAR Methods**). Repeated electrical stimulation of L4 *in*
205  *vitro* is sufficient to depress EPSCs recorded in L2/3 (L4: P2/P1 = 0.82 ± 0.02, P5/P1 = 0.75 ± 0.03, n =
206  14 cells; **Figure 4E**). Although L4 electrical stimulation could also activate non-L4 axons passing through
207  L4, direct optogenetic activation of L4 neurons at the same frequency depresses EPSCs to a similar

208    extent (**Figure S4**). In contrast, L2/3 excitatory inputs onto the same cells depress significantly less
209    (P2/P1 = 0.91 ± 0.02, P5/P1 = 0.88 ± 0.04; two-way ANOVA: main effect of input layer, p < 0.001; **Figure**
210    **4F**). Thus, adaptation in V1 L2/3 neurons likely arises from short-term depression at specific excitatory
211    synapses originating from L4 neurons.

212

213    *Activation of L4, but not L2/3, is sufficient to drive adaptation in vivo*

214          To test whether activation of L4 is sufficient to drive adaptation *in vivo*, we made extracellular
215    recordings from transgenic mice expressing ChR2 in L4 (**Figure 5A**). Units were identified as L4 or L2/3
216    neurons based on waveform position relative to layer boundaries determined by the visually-evoked
217    current source density (**Figure S5**). In agreement with the *in vitro* results, 0.1 s of repeated optogenetic
218    activation of L4 neurons significantly decreases responses in L2/3 neurons, but not L4 neurons (**Figure**
219    **S6A-C**). In order to investigate the interaction between optogenetic activation and subsequent visually
220    driven responses, we used a 0.5 s sinusoidal light stimulus (**Figure S6D-F**). Trials were randomly
221    interleaved to present visual stimulation alone or visual stimulation preceded by optogenetic stimulation
222    of L4 (**Figure 5B**). We then compared adaptation induced by visual stimuli under control conditions
223    ($Test_{control}$/$Baseline_{control}$: "Visual adapt"; **Figure 5C**) and adaptation induced by optogenetic stimulation
224    ($Baseline_{opto}$/$Baseline_{control}$: "Opto. adapt" **Figure 5C**).

225          Consistent with previous work, on control trials V1 neurons in L2/3 are suppressed by visual
226    adaptation at short ISIs (L2/3 Visual adapt [0.25 s ISI]: 0.64 ± 0.04; n = 34 cells; **Figure 5D-E**) while
227    neurons in L4 undergo significantly less adaptation[20] (L4 Visual adapt [0.25 s ISI]: 0.82 ± 0.04; n = 47
228    cells; p < 0.001, unpaired t-test). Optogenetic activation of L4 neurons generates effects similar to visual
229    adaptation in both L2/3 and L4: baseline visual responses are more strongly reduced in L2/3 (L2/3 Opto.
230    adapt [0.25 s ISI]: 0.60 ± 0.07; n = 34 units; **Figure 5D-E**) than in L4 (L4 Opto. adapt [0.25 s ISI]: 0.81 ±
231    0.05; n = 47 units; p < 0.001, unpaired t-test). The time scale of recovery from optogenetic adaptation is
232    also similar to recovery from visual adaptation. Across all ISIs, optogenetic adaptation is indistinguishable
233    from visually evoked adaptation (two-way ANOVA, effect of stimulation type: L2/3 p = 0.93, L4 p = 0.47).
234    Notably, in a subset of L2/3 neurons that are not activated by L4 optogenetic stimulation, visual responses
235    are unaffected even shortly after ChR2 activation (L2/3 Opto. adapt [0.25 s ISI]: laser active neurons [n
236    = 26 units] vs not laser active neurons [n = 8 units], p < 0.001; **Figure S6G**). L4 neurons showed a similar,
237    but not significant trend (L4 Opto. adapt [0.25 s ISI]: laser active neurons [n = 39 units] vs not laser active
238    neurons [n = 8 units], p = 0.11; un-paired t-test; **Figure S6H**). Thus, activation of L4 is sufficient to
239    reproduce the magnitude, recovery, and layer-specific effects of visual adaptation.

240          Although optogenetic stimulation of L4 is sufficient to drive adaptation, it is possible that similar
241    effects are produced through a non-overlapping, parallel mechanism to visual adaption. Because the
242    effects of visual adaptation saturate quickly with additional stimulus presentations (**Figure 3B, 4F** and
243    **5C**), we reasoned that if optogenetic stimulation and visual adaptation act through the same mechanism,
244    stimulation of L4 should also reduce subsequent visual adaptation[20]. Conversely, persistence of strong
245    visual adaptation would indicate engagement of distinct mechanisms. To test this, we compared the
246    magnitude of visual adaptation at short (0.25 s) ISIs in control trials versus after optogenetic stimulation
247    ($Test_{opto}$/$Baseline_{opto}$: "Opto. visual adapt"; (**Figure 5C**). We find that following optogenetic stimulation of
248    L4, responses to the test stimulus show little effect of visual adaptation (L2/3 $Test_{opto}$ vs $Baseline_{opto}$ [0.25
249    s ISI]: n = 24 units; p = 0.49). Consequently, visual adaptation in L2/3 is significantly reduced following
250    optogenetic adaptation (L2/3 Visual adapt vs Opto. visual adapt [0.25 s ISI] p < 0.001, paired t-test);

251 **Figure 5F-G**). The occlusion of adaptation in L2/3 by stimulation of L4 indicates that adaptation evoked
252 by visual and optogenetic stimulation likely act through the same mechanism.

253   While optogenetic stimulation of L4 is sufficient to induce visual adaptation in L2/3, this stimulation
254 also activates recurrent and feedback inputs within L2/3, which could generate the effects we observe.
255 To test whether activation of L4 is necessary for driving visual adaptation, we used *in utero*
256 electroporation to selectively express ChR2 in L2/3 pyramidal cells and made extracellular recordings
257 under the same experimental conditions (**Figure 6A-B**). Firing rates in L2/3 are not reduced following
258 L2/3 stimulation (Opto. adapt [0.25 s ISI]: $1.05 \pm 0.06$; n = 27 units; p = 0.94, paired t-test; **Figure 6C-D**),
259 and the magnitude of this effect is significantly smaller than occurs in response to both visually evoked
260 adaptation (p < 0.001; paired t-test) and L4 stimulation (p = 0.007; unpaired t-test). In addition, unlike L4,
261 L2/3 stimulation does not occlude visual adaptation (Opto. visual adapt [0.25 s ISI]: $0.68 \pm 0.08$; n = 27
262 units; $Test_{opto}$ vs $Baseline_{opto}$ [0.25 s ISI]: p = 0.002, paired t-test; **Figure 6E-F**). Overall, our results are
263 consistent with the preferential short-term depression at L4 inputs to L2/3 observed *in vitro*. We find that
264 activation of L4, but not L2/3, can recapitulate the effects of visual adaptation. Thus, activation of the L4
265 to L2/3 synapse is both necessary and sufficient for visual adaptation in L2/3.

266

267 *Rapid adaptation results from short-term depression at L4 to L2/3 synapses*

268   Short-term depression is associated with activity-dependent depletion of readily releasable
269 vesicles at high release probability (Pr) synapses[11]. To test whether short-term depression at L4
270 synapses is necessary for rapid adaptation, we optogenetically manipulated Pr using the modified
271 mosquito opsin, eOPN3, which enables reversible inhibition of vesicle release[34]. With green light
272 exposure, eOPN3 activates a $G_{i/o}$ pathway to inhibit calcium channels and SNARE complex formation,
273 reducing vesicle release and decreasing depletion[11,34]. Thus, we can use eOPN3 to decrease Pr
274 selectively at L4 synapses and test whether this also decreases short-term depression and rapid
275 adaptation.

276   We expressed eOPN3 in L4 neurons by injecting a Cre-dependent viral construct in Scnn1a-Tg3-
277 Cre mice and confirmed its effects using *in vitro* whole-cell recordings of EPSCs in L2/3 neurons (**Figure
278 7A**). We used a small spot of green light positioned over the recorded cell to activate eOPN3 expressed
279 at L4 axon terminals and measured EPSCs evoked with a 4 Hz train of electrical stimulation in L4 (**Figure
280 7B**). To ensure the effects were specific to eOPN3 activation in L4 axons, on alternating trials we recorded
281 EPSCs evoked by placing a second stimulation electrode in L2/3, ~100 μm from the recorded cell to
282 avoid the ascending L4 axons. Due to the relatively slow off-kinetics of eOPN3, we performed these
283 experiments in a block-wise structure (**Figure 7A**). After a block of control trials, the eOPN3 block was
284 initiated with 10 s of green light exposure with an additional 0.5 s of green light exposure preceding each
285 trial in the block. We then returned to control conditions to measure the time course of recovery.

286   Consistent with a reduction in Pr, activation of eOPN3 significantly reduces the amplitude of
287 EPSCs elicited by L4 electrical stimulation (**Figure 7C;** $P1_{eOPN3}/P1_{Baseline}$: $0.63 \pm 0.03$, p < 0.001, paired
288 t-test), increases the paired-pulse ratio (p = 0.02; **Figure 7D**), and increases the coefficient of variation
289 (p = 0.02; **Figure 7E**). In contrast, EPSCs evoked by L2/3 electrical stimulation are significantly less
290 suppressed than L4 stimulation ($P1_{eOPN3}/P1_{Baseline}$: $0.89 \pm 0.18$, L4 vs L2/3: p = 0.003, paired-t-test; **Figure
291 7C**) and have no significant change in paired-pulse ratio (p = 0.69, paired t-test; **Figure 7D**) or coefficient
292 of variation (p = 0.32; **Figure 7E**). Following the eOPN3 activation block, the amplitude of evoked L4
293 EPSCs recover over a few minutes ($\tau = 3.34$ min). The reversible and selective nature of the suppression
294 suggests an effect on vesicle release, rather than unrelated instabilities during recording. Thus,

295 optogenetic inhibition of L4 terminals can reduce short-term depression and vesicle depletion in a
296 pathway-specific manner.

297       We next determined whether decreasing Pr and short-term depression at L4 synapses prevents
298 rapid adaptation of visual responses *in vivo*. To test this, we recorded V1 neurons extracellularly while
299 presenting pairs of static gratings (0.25 s ISI), and activated eOPN3 using the same block-wise paradigm
300 as we validated *in vitro,* illuminating L4 axons in V1 with green light via an optic fiber outside the brain
301 (**Figure 8A-B**)**.** To quantify the effect of this manipulation on visual responses, we compared responses
302 to the baseline stimulus on control and eOPN3 activation trials (**Figure 8C** and **S7A**). This manipulation
303 produces a range of effects on stimulus-evoked firing rates: neurons with less than a 20% change in firing
304 rate were categorized as stable, while neurons that decreased or increased by more than 20% as
305 inhibited or facilitated, respectively (**Figure 8D**). Consistent with our manipulation largely targeting L4 to
306 L2/3 synapses, most neurons in L2/3 are inhibited following eOPN3 activation (inhibited: 67/105; stable:
307 28/105; $p < 0.001$, Chi-squared test; **Figure 8E**), whereas most neurons in L4 are stable (inhibited: 18/61;
308 stable: 34/61; $p = 0.003$, Chi-squared test;).

309       If suppression of neurons in L2/3 is indicative of decreased Pr at L4 inputs to those neurons,
310 visual adaptation should be most affected in neurons L2/3 neurons inhibited by eOPN3 activation. Indeed,
311 inhibited neurons in L2/3 undergo significantly less visual adaptation after eOPN3 activation ($p < 0.001$,
312 paired t-test; **Figure 8F, H-I**). In comparison, there is no change in the adaptation of stable neurons in
313 L2/3 ($p = 0.99$; **Figure 8G-I**), inhibited neurons in L4 ($p = 0.21$; **Figure S7B-C**), or stable neurons in L4
314 ($p = 0.45$). These effects cannot be explained by non-specific effects of the laser, as green light activation
315 of L4 neurons expressing only a fluorophore has no significant effect on visually-evoked firing rates of
316 L2/3 neurons (n = 35 cells; response to baseline stimulus- $p = 0.75$; paired t-test; **Figure S7D-E**) or the
317 degree of adaptation ($p = 0.34$). Nor could these effects be explained solely by reduced visual responses
318 in L2/3 induced by eOPN3, as L2/3 neurons exhibit a comparable reduction of visually-evoked firing with
319 a decrease in stimulus contrast (40% vs 80% contrast: normalized FR- 0.68 ± 0.06; n = 29 cells; $p <$
320 0.001; paired t-test; **Figure S8**) with no significant effect on adaptation ($p = 0.45$; two-way ANOVA, effect
321 of baseline contrast). Together, our results indicate that short-term depression at high Pr L4 to L2/3
322 synapses in V1 is necessary for the effects of visual adaptation.

323

324 **Discussion**

325       We have shown that synaptic depression at feedforward synapses within primary visual cortex
326 can explain stimulus-specific adaptation of visually-evoked responses. Our results demonstrate that
327 features of rapidly changing visual stimuli are stored at the level of synapses through activity-dependent
328 modulation of synaptic efficacy. Moreover, the effects of this modulation reduce sensitivity to repeated
329 stimulus features, potentially serving to improve efficiency of stimulus encoding.

330

331 *Direct evidence for a synaptic depression mechanism in adaptation*

332       Short-term synaptic plasticity is a fundamental feature of the nervous system that can transform
333 physically static synapses into dynamic filters of presynaptic activity[11,35,36]. Previous *in vitro* results from
334 electrical stimulation[12], two-photon optogenetic input mapping[32], and paired recordings[33,37] have found
335 that short-term depression is the dominant form of plasticity at L4 to L2/3 synapses in V1. In contrast to
336 cell-intrinsic mechanisms involved at long timescales of continuous visual experience, the effects of
337 synaptic depression can be engaged with brief, transient stimulation. Using whole-cell recordings of L2/3

338    neurons *in vitro* and *in vivo* we demonstrate that changes in synaptic inputs from L4 can explain the long-
339    lasting and stimulus-specific nature of rapid adaptation of spike output.

340    Many studies have hinted that synaptic depression plays a role in generating adaptation to
341    repeated stimulus presentations *in vivo*[10,24,25,27,38–43]. In cat visual cortex, repeated electrical stimulation
342    of LGN neurons produces suppression of excitation and inhibition in cortical neurons[27]. Similarly,
343    balanced reduction of excitation and inhibition has been observed during adaptation to whisker
344    stimulation in barrel cortex and clicks in auditory cortex[24,38]. Although these findings are consistent with
345    synaptic depression, these experiments did not directly test the role of short-term plasticity. In this study,
346    we leverage cell-type specific *in vitro* and *in vivo* optogenetic manipulations to directly manipulate
347    synaptic transmission at L4 neurons and found that activation of L4 inputs to L2/3 is both necessary and
348    sufficient for producing the effects of visual adaptation. Notably, while we find that the majority of
349    adaptation can be accounted for by depression at this cortical synapse, synaptic depression has been
350    reported at both retinogeniculate and thalamocortical synapses[42,44–47]. These discrepancies could
351    originate from differences in spontaneous activity that depend on state (awake vs anesthetized) and
352    preparation (*in vivo* vs *in vitro*). Spontaneous thalamic activity depends on the type and depth of
353    anesthesia, and will therefore modulate the degree of depression at thalamocortical synapses. Similarly,
354    higher overall levels of spontaneous activity *in vivo* shift these synapses closer to saturated levels of
355    depression at rest compared to *in vitro*[44,48,49]. Thus, the degree of adaptation along the visual hierarchy
356    is not a fixed property of these synapses, but instead strongly depends on brain state. Our results
357    therefore provide insight to relevant mechanisms that govern visual processing in the alert animal.

358

359    *Rapid adaptation is not associated with increased inhibition*

360    Another mechanism that has been proposed to mediate stimulus-specific adaptation is increased
361    inhibition. One model for increased inhibition proposes that it arises via differential synaptic plasticity at
362    excitatory synapses from pyramidal cells to inhibitory interneurons, or from inhibitory synapses from
363    interneurons to pyramidal cells[50–54]. In particular, facilitation of excitatory inputs onto somatostatin-
364    expressing (SOM) interneurons is thought to sensitize them to repeated or prolonged stimulus
365    presentations[55–57]. Indeed, manipulation of SOM interneurons selectively affects responses to frequent,
366    but not rare stimuli in visual and auditory cortex[26,58,59].

367    Contrary to this model, our recordings indicate that the adapter stimulus does not generate long-
368    lasting inhibition in L2/3 neurons, nor does inhibition increase in response to the test stimulus. Instead,
369    the magnitude of excitation and inhibition are tightly linked across stimulus conditions and undergo similar
370    degrees of adaptation. The most straightforward explanation for this balanced decrease of excitation and
371    inhibition is through a single effect of short-term depression of excitatory L4 to L2/3 synapses onto both
372    cell types. This model is further supported by the orientation specificity of adaptation of excitation and
373    inhibition which more closely matches the tuning of excitatory than of inhibitory neurons. Moreover, we
374    find that FS interneurons undergo a similar degree of adaptation as neighboring RS cells. Thus,
375    adaptation of inhibition is likely driven by short-term depression of the excitatory inputs onto L2/3
376    interneurons rather than short-term dynamics of their output inhibitory synapses. Notably, *in vitro*
377    recordings reveal a strong degree of short-term depression at these inhibitory synapses[50,60–62]. Thus, it
378    is surprising that there is no clear contribution of short-term plasticity at this synapse to driving additional
379    adaptation of inhibition. We propose that the high firing rates of interneurons *in vivo* may put their
380    synapses in a tonically depressed state, rendering them stable across a range of stimulus intervals[44,63].

381    It is likely that our whole-cell recordings *in vivo* have limited space clamp and therefore may be
382 underestimating the contribution of dendritic inhibition. However, we saw no dependence of the degree
383 of adaptation of either excitatory or inhibitory currents on series resistance (**Figure S2**), arguing against
384 a role for facilitating dendritic inhibition. Instead, the observed decrease in total synaptic input is sufficient
385 to explain the changes observed in spike output, rendering increased inhibition unlikely to explain
386 adaptation at this time scale of induction and recovery.
387
388    *Distinct time scales and perceptual effects of adaptation*
389    A short-term depression mechanism predicts a distinct set of computational capacities compared
390 to cell-intrinsic fatigue. At any moment, a single neuron's response is determined by the sum of thousands
391 of synaptic inputs, meaning that independent gain changes at each of these inputs can greatly increase
392 possible modifications of activity with adaptation[64–66]. Modeling studies predict that short-term depression
393 normalizes the strength of individual inputs to each afferent's mean firing level to maintain postsynaptic
394 sensitivity to changes in presynaptic firing[36,66]. Our results indicate that adaptation selectively regulates
395 L4 to L2/3 inputs, a key cortical, feedforward synapse in visual processing. Input-specific depression at
396 L4 but not L2/3 inputs to L2/3 neurons could shift the relative balance of information flow from feedforward
397 to recurrent connections. Further, the cortical site of adaptation (as opposed to at the thalamocortical
398 synapse) allows for adaptation to be orientation-specific. The stimulus specificity of short-term depression
399 can also be extended to other forms of cortically-computed stimulus selectivity (e.g. phase or spatial
400 frequency) to reduce redundant encoding across multiple features[67,68]. Synaptic depression has also
401 long been proposed to act as a low-pass filter for cortical processing[12,35,69]. Thus, in addition to enabling
402 cortical circuits to adjust to recent history, this form of adaptation may also shape temporal integration by
403 limiting the rate at which cortical circuits can follow rapidly fluctuating visual inputs, setting the threshold
404 for flicker-fusion[70,71].
405    Moving forward, we can begin to connect the diversity of perceptual effects of adaptation to the
406 diversity of biological mechanisms that affect activity over time. Perceptual effects of adaptation can vary
407 depending on duration even in response to a visual stimulus with the same spatial features. Our data
408 indicate that this could arise through complementary mechanisms that ebb and flow on different time
409 scales within the same neurons. This is consistent with studies that have identified multiple timescales of
410 adaptation within single neurons that vary by orders of magnitude[9,10]. As a result, visual perception is
411 shaped by concurrent dependencies on stimulus history that vary in their computational capacities.
412 Another interpretation of these multiple forms of adaptation is as a series of mechanisms that work
413 together to reduce activity in stages—if synaptic depression is not sufficient to reduce firing rates, cell-
414 intrinsic hyperpolarization can reduce responses over longer periods of elevated excitation. Notably, this
415 will come at the expense of stimulus specificity, but may be necessary to maintain cortical homeostasis.
416 Indeed, prior studies using a greater number of stimulus presentations have identified both orientation
417 specific and nonspecific components of adaptation[10,20]. Thus, future work will be important for
418 understanding the nature of interactions between distinct mechanisms in individual neurons.
419
420    In summary, we have linked a well-studied synaptic mechanism to the *in vivo* phenomenon of
421 adaptation at rapid timescales in V1. While distinct, synaptic and cell-intrinsic mechanisms need not be
422 mutually exclusive and likely co-exist within single neurons[9,10,39]. Our findings provide long sought-after
423 evidence for a synaptic depression mechanism at intracortical synapses that generates sensory
424 adaptation and sparsens representations. Given the similarity of cortical structure and observed features

425 of rapid adaptation across sensory areas, this mechanism could be applicable across many stimulus
426 modalities[9,72–74]. Release probability is an inherent property at chemical synapses in the brain[11]; thus,
427 molecular machinery and neuromodulators that affect Pr can regulate synaptic transmission at a given
428 set of synapses over time (as we've studied here), but could also specialize the dynamics of responses
429 across different brain areas, or even different species. Therefore, studies of short-term plasticity at
430 synapses further along the visual hierarchy[20], in different behavioral contexts[75], sensory areas[9], or
431 species, could all generate insights into how fundamental attributes of synapses shape the neural code.

432
433

440
441 Author Contributions
442
443 Conceptualization: J.Y.L. and L.L.G.; Formal Analysis: J.Y.L.; Investigation: J.Y.L.; Data Curation: J.Y.L.;
444 Writing- Original Draft: J.Y.L.; Writing- Review and Editing: J.Y.L. and L.L.G; Visualization: J.Y.L.;
445 Supervision: L.L.G.; Funding Acquisition: J.Y.L. and L.L.G.

446
447 Declaration of Interests:
448
449 The authors declare no competing interests.

450
451 **Figure Legends**
452
453 **Figure 1. Adaptation suppresses stimulus-evoked responses in L2/3 neurons without affecting**
454 **cell-intrinsic properties. A.** Left: Recording setup and stimulus paradigm. Animals are head-fixed on a
455 treadmill and membrane potential (Vm) of L2/3 neurons is recorded with a glass pipette. Two stimuli
456 (baseline and test; 0.1 s) are separated by an inter-stimulus interval (ISI) varying from 0.25 to 4 s. Right:
457 Membrane potential is separated into the stimulus-evoked firing rate (black) and stimulus-evoked post-
458 synaptic potential (blue; PSP). **B.** Top: Membrane potential from an example cell during a 0.25 s ISI trial.
459 Grey shading indicates stimulus presentation. Middle: Raster plot of spike output during 0.25 s (light
460 purple) and 4 s (dark purple) ISI trials and binned peri-stimulus spike histogram (PSTH). Bottom:
461 Subthreshold membrane potential during baseline (left) and test stimulus presentations at 0.25 s (middle)
462 and 4 s (right) ISIs. **C.** Left: Average normalized firing rate (FR; test/baseline) as a function of ISI for
463 individual cells (gray lines) and all cells (black circles; n = 13). Error is SEM across cells. Black line is an
464 exponential fit ($\tau$ = 0.82 s). Right: Same as left, for average normalized PSP amplitude ($\tau$ = 0.79 s). **D.**
465 Average membrane potential preceding baseline and test stimuli for individual cells in 0.25 s ISI trials.
466 Black dot is mean across cells. Error bar is SEM across cells. **E-G.** Same as **D** for spike threshold (**E**),
467 membrane variance (**F**), and PSP amplitude (**G**).

468
469 **Figure 2. Adaptation drives a balanced reduction in stimulus-evoked excitation and inhibition. A.**
470 Left: Schematic of recording setup for measuring excitatory and inhibitory currents (EPSCs and IPSCs)
471 in L2/3 neurons. Right: Single trial voltage traces from an example cell held at -70 mV (black) and +10

472   mV (red), to measure EPSCs and IPSCs respectively. **B.** Grand average of stimulus-evoked EPSCs and
473   IPSCs across all cells (n = 10) in response to baseline and test stimuli for all ISIs. Shaded error is SEM
474   across cells. **C.** Average normalized current amplitudes (test/baseline) for EPSCs (black) and IPSCs
475   (red) for individual cells (small dots) and across all cells (large dots). Curve is exponential fit to the
476   average across cells for each current type. Error bar is SEM across cells. **D.** Ratio of excitation to
477   inhibition (E/I) for the baseline and test stimulus in 0.25 s ISI trials. Grey lines are individual cells, black
478   line is average across cells, error is SEM across cells. **E.** Comparison of visual adaptation in 0.25 s ISI
479   trials in putative pyramidal cells (RS, black) and inhibitory interneurons (FS, gray), obtained from
480   extracellular recordings (**Figure S3**). Error bar is SEM across units.
481
482   **Figure 3. Changes in synaptic input are selective to previously activated synapses. A.** Schematic
483   of proposed model of synapse-specific effect of adaptation on excitatory inputs from L4 to L2/3. This
484   generates orientation-selective decrease of synaptic inputs to both excitatory and inhibitory L2/3 neurons.
485   Color of axons correspond to L4 inputs to L2/3 synapses tuned to vertical (black) versus horizontal (blue)
486   orientations. Line thickness represents strength of inputs. **B.** Top: Visual stimulus paradigm with repeated
487   presentation of the same stimulus orientation (baseline and test 1-4) followed by an orthogonal orientation
488   (test 5). Middle: Average stimulus evoked EPSCs (black) and IPSCs (red) for an example cell. Bottom:
489   Average normalized current (test/baseline) for all cells (n = 8). Response to the orthogonal orientation is
490   normalized to its own baseline. Error bar is SEM across cells. **C.** Left: Schematic of stimuli presented to
491   measure the tuning width of adaptation. Test orientation was kept constant while the baseline orientation
492   varied. Right: Average normalized current (test/baseline, where the baseline is the same orientation as
493   the test) as a function of similarity between baseline and test stimuli for EPSCs and IPSCs for all cells (n
494   = 13). **D.** Average adaptation tuning curve fits from data in **C**. Shaded error is SEM across cells. Tuning
495   width (TW) is half-width at half-max. **E.** Average orientation tuning curve fits from extracellular recording
496   of V1 RS (black) and FS (gray) units.
497
498   **Figure 4. Excitatory inputs to L2/3 neurons decrease with repeated stimulation *in vitro*. A.**
499   Schematic of setup for recording EPSCs in L2/3 neurons during optogenetic stimulation of L4. Two 0.1 s
500   square pulses of blue light (baseline and test) were used to activate L4 neurons. **B.** Average traces during
501   baseline (dark blue) and test (light blue) stimuli from an example cell during 0.25 s (left) versus 4 s (right)
502   ISI trials. **C.** Average normalized EPSC amplitudes (test/baseline) as a function of ISI for each cell (gray)
503   and the across all cells (blue). Blue line is exponential fit to the average across cells. Dashed line is
504   exponential fit from EPSCs recorded *in vivo* in **Figure 2**. Error bar is SEM across cells (n = 11). **D.**
505   Schematic for recording EPSCs from a L2/3 pyramidal cell while electrically stimulating L4 or L2/3 inputs
506   on alternating trials. **E.** Average EPSCs from an example cell in response to stimulation of L2/3 (top;
507   gray) or L4 (bottom; black). **F.** Average EPSC amplitudes normalized to the first stimulus in response to
508   L2/3 (gray) and L4 (black) stimulation. Error bar is SEM across cells.
509
510   **Figure 5. Activation of L4 neurons is sufficient to recapitulate the effects of visual adaptation. A.**
511   Schematic of *in vivo* extracellular recording setup with optrode coupled to a 450 nm laser. **B.** Structure
512   of control trials (black) and ChR2 activation trials (blue). On control trials, baseline and test stimuli are
513   presented with varying ISI. On ChR2 activation trials, 0.5 s of sinusoidal blue light is used to activate L4
514   neurons optogenetically at varying intervals prior to baseline visual stimulus presentation. **C.** Visual
515   adaptation is quantified as the response to the test divided by the response to the baseline stimulus (gray
516   shaded box). Optogenetic adaptation is quantified as the response to the baseline stimulus in ChR2
517   activation trials divided by the response to the baseline stimulus in control trials (blue arrow). Optogenetic
518   visual adaptation is quantified as the response to the test stimulus divided by the baseline stimulus
519   following on ChR2 activation trials (blue shaded box). **D.** Average z-scored PSTH for L2/3 units during
520   baseline (black) and test (gray) stimuli in control trials and baseline stimulus in ChR2 activation trials
521   (blue; n = 34 units). Black line indicates stimulus presentation. Shaded error is SEM across unit. **E.**
522   Comparison of visual adaptation (black) and optogenetic adaptation (blue) in L2/3 (left) and L4 (right)

523    units. Green fill indicates optogenetic stimulation of L4. **F.** Average z-scored PSTH for L2/3 units during
524    baseline (blue) and test (light blue) stimuli in L4 ChR2 activation trials. **G.** Visual adaptation (black) and
525    Optogenetic visual adaptation (blue) with 0.25 s ISI at increasing intervals after L4 stimulation (0.25 s, 1
526    s, 4 s). Normalized firing rate is calculated relative to baseline visual response in control trials (horizontal
527    dashed line). Error bar is SEM across units.
528
529    **Figure 6. Activation of L2/3 neurons does not recapitulate the effects of visual adaptation. A.** Left:
530    Schematic of *in vivo* extracellular recording setup in mice expressing ChR2 in L2/3 neurons. Right:
531    expression of ChR2-mRuby in L2/3 neurons following *in utero* electroporation. Scale bar is 100 μm. **B.**
532    Structure of control trials (black) and ChR2 activation trials (blue). **C.** Average z-scored PSTH for L2/3
533    units during baseline (black) and test (gray) stimuli in control trials and baseline stimulus in ChR2
534    activation trials (blue; n = 27 units). Black line indicates stimulus presentation. Shaded error is SEM
535    across units. **D.** Comparison of visual adaptation (black) and optogenetic adaptation (blue) in L2/3 (left)
536    and L4 (right) units. Red fill indicates optogenetic stimulation of L2/3. **E.** Average z-scored PSTH for L2/3
537    units during baseline (blue) and test (light blue) stimuli in L2/3 ChR2 activation trials. **F.** Visual adaptation
538    (black) and Optogenetic visual adaptation (blue) with 0.25 s ISI at increasing intervals after L2/3
539    stimulation (0.25 s, 1 s, 4 s). Normalized firing rate is calculated relative to baseline visual response in
540    control trials (horizontal dashed line). Error bar is SEM across units.
541
542    **Figure 7. Activation of eOPN3 in L4 terminals reduces probability of release at inputs onto L2/3**
543    **neurons. A.** Left: Schematic of *in vitro* recording setup for recording EPSCs in L2/3 neurons while
544    electrically stimulating L4 or L2/3. eOPN3 expressed in L4 neurons is activated with green light over L4
545    terminals in L2/3. Right: Example image of viral expression pattern. Scale bar is 100 μm. **B.** EPSCs from
546    an example cell in response to L4 stimulation during first (P1) and second (P2) stimuli in a train (4 Hz),
547    either before (black) or after eOPN3 activation (green). **C.** Average time course of normalized P1 EPSC
548    amplitudes following L4 (left) or L2/3 (right) stimulation aligned to the time of eOPN3 activation (n = 14
549    cells). Vertical green lines indicate eOPN3 activation trials: induction of 10 s of pulsed green light prior to
550    visual stimulus presentation, followed by a top-up of 0.5 s of pulsed green light prior. Black curve is
551    exponential fit to recovery. Shaded error is SEM across cells. **D.** Paired pulse ratio (PPR) during L4 or
552    L2/3 stimulation for individual cells (gray lines) and the average of all cells (black) in control (white) and
553    after eOPN activation (green). Error bar is SEM across cells. **E.** Same as **D**, for coefficient of variation.
554
555    **Figure 8. Decreasing probability of release at L4 terminals decreases visual adaptation *in vivo*. A.**
556    Schematic of recording setup and eOPN3 expression with green light illumination outside of the brain. **B.**
557    Block-wise trial structure for measuring effects of eOPN3 activation on visual adaptation. Visual stimuli
558    are always presented with 0.25 s ISI. eOPN3 activation block consist of an induction of 10 s of pulsed
559    green light prior at the start of the block, followed by a top-up of 0.5 s of pulsed green light prior to visual
560    stimulus presentation on each trial. **C.** PSTHs for two example units in control (black) and eOPN3
561    activation (green) trials. Δ FR is calculated as the change in peak stimulus-evoked response. **D.**
562    Distribution of change in visually-evoked responses to the baseline stimulus in L4 (pink; n = 61) and L2/3
563    (gray; n = 105) units. Vertical solid lines indicate thresholds for categorization as inhibited (< 0.8), stable
564    ($\geq$ 0.8 and $\leq$ 1.2), or facilitated (> 1.2). **E.** Percent of units categorized as inhibited, stable, or facilitated
565    in L2/3 and L4. **F.** Average z-scored PSTH of inhibited L2/3 units (n = 65) in response to baseline (dark)
566    and test (light) stimuli during control trials (left, black) and during eOPN3 activation trials (right, green).
567    Black line indicates stimulus presentation. Shaded error is SEM across units. **G.** Same as **F**, for stable
568    L2/3 units (n = 28). **H.** Comparison of normalized response (test/baseline) in control and eOPN3
569    activation trials, for all L2/3 units colored by categorization in **E**. **I.** Average normalized response for
570    inhibited (dark green) and stable (light green) units in L2/3. Error bar is SEM across units.

**STAR Methods**

**Key Resources Table**

| REAGENT or RESOURCE | SOURCE | IDENTIFIER |
|---|---|---|
| **Bacterial and virus strains** | | |
| rAAV2/1&2.hSyn.SIO-eOPN3-mScarlet | Addgene | 125713 |
| AAV1.CAG.Flex.tdTomato.WPRE.bGH | Addgene | 51503 |
| **Deposited data** | | |
| Data and code for analysis | This paper | 10.6084/m9.figshare.21675056 |
| **Experimental models: Organisms/strains** | | |
| Scnn1a-Tg3-Cre | Jackson Labs | 009613 |
| Ai32 | Jackson Labs | 012569 |
| CBA | Jackson Labs | 000654 |
| **Recombinant DNA** | | |
| pCAG-ChR2-mRuby | Addgene | 109125 |
| **Software and algorithms** | | |
| ImageJ | NIH | https://micro-manager.org |
| Micromanager | NIH | https://imagej.nih.gov/ij/ |
| MWorks | MWorks | http://mworks-project.org |
| pClamp 10 Software Suite | Molecular Devices | N/A |
| MATLAB | Mathworks | https://www.mathworks.com |
| **Chemicals** | | |
| Fast Green | Sigma Aldrich | F7252 |
| Fluoromount G | Invitrogen | 00-4959-52 |
| DiO | Invitrogen | V22886 |
| NBQX | Tocris Bioscience | Cat #: 1044; CAS: 479347-86-9 |
| D-APV | Tocris Bioscience | Cat #: 0106; CAS: 79055-68-8 |
| Dental Cement | C&B Metabond | S380 |

**RESOURCE AVAILABILITY**

*Lead contact*

Further information and requests for resources and reagents should be directed to Lindsey Glickfeld (glickfeld@neuro.duke.edu).

*Materials availability*

No new reagents were generated as a result of this study.

*Data and code availability*

- All electrophysiology data included in the manuscript figures is available on Figshare. A link is provided in the *Key resources table.*

591
592 • All original code needed to generate the manuscript figures is available on Figshare. A link is
593 provided in the *Key resources table.*
594
595 • Any additional information required to reanalyze the data reported in this paper is available from
596 the lead contact upon request.
597

598 **EXPERIMENTAL MODEL AND SUBJECT DETAILS**
599

600 *Animals.* All procedures conformed to standards set forth by the National Institutes of Health Guide for
601 the Care and Use of Laboratory Animals, and were approved by the Duke University's Animal Care and
602 Use Committee. Mice were housed on a normal 12:12 light-dark cycle. Data in this study were collected
603 from 74 mice (35 female). For experiments involving selective expression in layer 4 V1 neurons, we used
604 Cre-positive offspring from Scnn1a-Tg3-Cre mice (Jackson Labs #009613) crossed with either Ai32
605 (Jackson Labs #012569, n = 15), or CBA (Jackson Labs, #000654, n = 18). We also used offspring from
606 Scnn1a-Tg3-Cre and CBA mice for *in utero* electroporation (n = 11) but did not select for Cre expression.
607 All other experiments did not require cell-type specific expression; thus, mice were a mix of genotypes (n
608 = 32). Transgenic mice were heterozygous and bred on a C57/B6J background (Jackson Labs #000664)
609 with up to 50% CBA/CaJ (Jackson Labs #000654). *In vivo* electrophysiology experiments used mice 6-
610 22 weeks old and *in vitro* electrophysiology experiments used mice 4-12 weeks old. At the time of viral
611 injection, mice were at least 4 weeks old.
612

613 **METHOD DETAILS**
614

615 Surgical Procedures
616

617 *Intracranial viral injections.* Burrhole injections of viral constructs [rAAV2/1&2.hSyn.SIO-eOPN3-mScarlet
618 (Addgene 125713 diluted to 6 x $10^{12}$ viral genomes/mL) or AAV1.CAG.Flex.tdTomato.WPRE.bGH
619 (Addgene 51503; diluted to 3 x $10^{12}$ viral genomes/mL)] were used to selectively express opsins and
620 control fluorophores in layer 4. Mice were anesthetized with isoflurane and positioned in a stereotax (Kopf
621 Instruments). Meloxicam (5 mg/kg) was administered subcutaneously and bupivacaine (5 mg/kg) was
622 administered locally prior to incision. After the skull was exposed, a small hole was drilled -2.6 mm lateral
623 from lambda and directly anterior to the lambdoid suture targeting the posterior and medial aspect of the
624 primary visual cortex (V1). Injection micropipettes were pulled from glass capillary tubes (1B100F-4,
625 World Precision Instruments) and backfilled with virus and then mineral oil and mounted on a Hamilton
626 syringe. The pipette was lowered into the brain and pressure injected at two depths using an
627 UltraMicroPump (World Precisions Instruments; 2 x 100 nL; -350 µm and -450 µm from the surface). We
628 waited between 4.5-7 weeks for viral expression for both *in vitro* and *in vivo* electrophysiology and
629 confirmed expression *post hoc.*
630

631 *In utero electroporation.* Embryos from timed-pregnant CBA female mice (E15.5-16.5) mated to Scnn1a-
632 Tg3-Cre males were used to obtain expression in layer 2/3. Meloxicam was administered pre-operatively
633 (1 mg/mL, 5 mg/kg; subcutaneous). Animals were maintained under anesthesia (2.5% isoflurane), the
634 abdomen was cleaned with ethanol and then swabbed with iodine. An incision was made in the skin and
635 then in the abdominal wall, then covered in a drape made with sterile surgical gauze. Uterine horns were
636 carefully removed and kept moist with warm PBS throughout the surgery. Embryos were injected with
637 plasmid mixture (1.5 µg/uL pCAG-ChR2-mRuby-ST in 0.5% Fast Green in UltraPure water, Addgene
638 109125) in the left ventricle using a glass micropipette pulled to a 70 µm beveled tip. After injection, a
639 series of voltage steps (five voltage pulses of 50 V at 1 Hz with each pulse lasting 50 ms) was applied to
640 each embryo using 5 mm round tweezertrodes (BTX, BTX ECM 830 ElectroSquarePorator). Paddles

641 were oriented to target V1. Embryos were gently returned to the abdomen in the same side that they
642 were removed from. The abdominal wall was sutured before applying bupivicane (5 mg/kg) and then
643 suturing the skin. Animals were allowed to recover on a heating pad until mobile. Strength and location
644 of expression was screened with trans-cranial fluorescence of mRuby following headpost implantation.
645
646 *Headpost implantation*. Mice were anesthetized with a mixture of ketamine/xylazine (ketamine: 50 mg/kg,
647 xylazine: 5 mg/kg; intraperitoneal) and isoflurane (1.2–2% in 100% $O_2$). Meloxicam was administered
648 pre-operatively (1 mg/mL, 5 mg/kg; subcutaneous). Using aseptic technique, a custom-made titanium
649 headpost was secured over V1 using clear dental cement (C&B Metabond, Parkell). Buprenex (0.05
650 mg/kg) and cefazolin (50 mg/kg) were administered post-operatively. Animals were allowed to recover
651 for at least 1 week prior to experiments.
652
653 Visual and optogenetic stimulus presentation.
654
655 Visual stimuli were presented on a 144-Hz (Asus) LCD monitor, calibrated with an i1 Display Pro (X-rite).
656 The monitor was positioned 21 cm from the contralateral eye. Visual stimuli were controlled with MWorks
657 (http://mworks-project.org). Circular gabor patches containing sine-wave gratings (30º diameter; 0.1
658 cycles per degree; 80% contrast) alternated with periods of uniform mean luminance (60 cd/m$^2$). Timing
659 of visual stimulus onset was measured for aligning neural data via a photodiode that directly measured
660 output from the LCD. All baseline and test stimuli were presented for 0.1 s, with inter-stimulus intervals
661 (ISIs) ranging from 0.25 s to 4 s and inter-trial interval of 8 s to allow for adequate recovery.
662
663 *ChR2 activation.* Control and ChR2 activation trials were randomly interleaved. Control trials consisted
664 of two vertically oriented static gratings separated by a 0.25, 1, or 4 s ISI. ChR2 activation trials consisted
665 of a sine-wave laser pulse (0.5 s, 20 Hz, 450 nm, Optoengine) followed by a grating (0.25, 1, or 4 s ISI).
666 In a subset of experiments, two static gratings (0.25 s ISI) were presented following ChR2 activation to
667 measure the effect on visual adaptation. The effect of serial ChR2 activation was also tested using brief
668 (0.1 s) square-wave pulses (**Figure S6A-C**).
669
670 *Stimulus specificity of adaptation*. Two protocols were used to test the stimulus specificity of adaptation.
671 1) Five repeated presentations of a static grating (baseline and test 1-4; 0.25 s ISI) followed by a
672 presentation of the orthogonal orientation (test 5). On randomly interleaved trials, the repeated and
673 orthogonal orientation were switched to obtain the baseline amplitude of both orientations. 2) Two
674 oriented gratings were presented with an ISI of 0.25 s. The test stimulus was the same across trials while
675 the baseline stimulus was varied from 0 to 90 degrees from the test in 22.5 degree increments.
676
677 *Orientation tuning.* Drifting gratings (2 Hz) moving in 16 directions (22.5 degree increments) were
678 presented for 1 s with an 8 s inter-trial interval to measure the orientation tuning of neurons.
679
680 *eOPN3 activation.* All trials consisted of two vertically oriented baseline and test stimuli separated by 0.25
681 s ISI. After 20 control trials, eOPN3 was activated with a square-wave laser pulse (10 s, 10 Hz, 530 nm,
682 Optoengine). We then tested the effect of eOPN3 over 20 trials with top-up activation (0.5 s, 10 Hz)
683 preceding visual stimulation on each trial. Recovery was measured during a subsequent 90-100 trials.
684 Each experiment contained 1-3 repeats of eOPN3 activation blocks.
685
686 *Contrast dependence of adaptation*. Two vertically oriented gratings were presented with an ISI of 0.25
687 s. The test stimulus was the same (80% contrast) across trials while the baseline stimulus was either 40
688 or 80% contrast.
689
690 Experimental Procedures
691

*In vivo retinotopic mapping.* For all *in vivo* electrophysiological recordings, V1 boundaries were first identified with retinotopic mapping with intrinsic signal imaging through the skull. The skull was illuminated with orange light (590 nm LED, Thorlabs), and unfiltered emitted light was collected using a CCD camera (Rolera EMC-2, Q Imaging) at 2 Hz through a 5x air immersion objective (0.14 numerical aperture (NA), Mitutoyo), using Micromanager acquisition software[76]. Drifting gratings (80% contrast, 2 Hz, 0.1 cpd) were presented for 2 s at 3 positions with a 4 s interstimulus interval. Collected images were analyzed in ImageJ to measure changes in reflectance at each position (dR/R; with R being the average of all frames) to identify V1.

*Preparation for in vivo electrophysiology.* Animals were habituated to head-fixation for 1-3 days prior to surgery. On the day of recording, animals were anesthetized with isoflurane and a small craniotomy (< 1 mm diameter) was made over a V1 location identified by intrinsic signal imaging. For extracellular recordings, a gold ground pin was inserted in an anterior portion (outside of visual areas) within the headpost and secured with dental cement. Damage to superficial cortex was minimized by drilling in brief bouts (< 1 s) and alternating drilling and cooling with chilled glucose-free HEPES-based artificial cerebral spinal fluid (ACSF; in mM: 141 NaCl, 2.5 KCl, 10 HEPES, 2 $CaCl_2$ 1.3 $MgCl_2$). A slit was made in the dura with a syringe and the craniotomy was kept covered with ACSF for the remainder of the experiment. Animals were allowed to recover on the running wheel for at least 45 minutes before recording. In a subset of experiments, recording was performed the day after the craniotomy or animals were used for up to 2 consecutive recording days. In these cases, the craniotomy was protected overnight with Dura-Gel (Cambridge NeuroTech) and dental cement, which were removed and replaced with ACSF prior to recording.

*In vivo whole-cell recordings.* Whole-cell recordings were performed using blind patch technique. A silver chloride ground pellet was placed in the recording well outside of the brain. Recording ACSF was wicked away from the craniotomy and a 3-5 MOhm glass micropipette was lowered until the pipette tip touched the brain (confirmed by appearance of a square pulse on the membrane test); this position was zeroed and the well was refilled with recording ACSF. All recordings were documented relative to this depth. The pipette was lowered to ~100 $\mu$m depth and then stepped in 1-2 $\mu$m increments until an increase in resistance was observed and pressure was released to form a G$\Omega$ seal. Cells recorded at 180-350 $\mu$m depths were considered to be within L2/3. For current clamp recordings, internal solution contained (in mM): 142 K-gluconate, 3 KCl, 10 HEPES, 0.5 EGTA, 5 phosphocreatine-di(tris), 5 phosphocreatine-$Na_2$, 3 Mg-ATP, 0.5 GTP; for voltage clamp recordings, internal solution contained (in mM): 125 Cs-methanesulfonate, 5 TEA-Cl, 10 HEPES, 0.5 EGTA, 4 Mg-ATP, 0.3 $Na_3$GTP, 8 phosphocreatine-di(tris), 3 NaCl. For voltage clamp recordings, EPSCs were recorded at -70 mV and IPSCs were recorded at +10 mV based on previous literature and our own calibration with ChR2 activation of interneurons *in vivo* (**Figure S2A**). Series resistance was monitored using -5 mV steps preceding each stimulus; recordings that reached >35 M$\Omega$ resistance or >20% change from baseline were discarded. The order of recording EPSCs and IPSCs was varied across experiments, and there was no relationship between the series resistance and the normalized current for either holding potential (**Figure S2B-C**; EPSCs p = 0.21, IPSCs p = 0.57).

  In a subset of recordings, a low resistance pipette (1 M$\Omega$) was filled with 3 M NaCl and lowered ~200 $\mu$m to measure local field potential and determine optimal stimulus position. Otherwise, optimal stimulus position was determined separately for azimuth and elevation by observing spikes or EPSCs in response to a flashing white bar (0.1 s on, 1 s off, 5 degree width). Following optimization of stimulus position, spikes and EPSCs were analyzed online to determine the preferred stimulus orientation.

*In vivo extracellular recordings.* Extracellular recordings were performed with a 32-site acute probe (A1x32-Poly2–5mm-50s-177-A32, NeuroNexus or H4, Cambridge NeuroTech). Probes were connected through an A32-OM32 adapter to a Cereplex Mu digital headstage (Blackrock Microsystems). Signals

742  were digitized at 30 kHz and recorded by a Cerebus multichannel data acquisition system (Blackrock
743  Microsystems). Probes were slowly lowered into the brain until all sites were inserted and allowed to
744  stabilize for 40–50 min before recording. For experiments involving localized viral expression, the probe
745  was painted with DiO (Thermo Fisher) to confirm with *post hoc* histology that the electrode tract was
746  within the expression region.
747      For optogenetic experiments, we used either a 450 nm or 532 nm laser (Optoengine) to activate
748  ChR2-expressing neurons or inhibit L4 terminals with eOPN3, respectively. Lasers were coupled to an
749  optic shutter and patch cable terminating in an optic fiber. For L2/3 ChR2 activation and eOPN3 inhibition
750  experiments, probes had attached optic fibers (200 μm core, 0.22 NA) that terminated 100 μm above the
751  surface of the brain. For L4 ChR2 stimulation, a tapered lambda fiber (100 μm core with 0.9 mm taper,
752  0.22 NA, Optogenix) was inserted in the brain aligned to the tip of the probe for enhanced light
753  transmission deeper in the brain. Laser power was calibrated to deliver 1 mW power at fiber tip for ChR2
754  activation and 1.2 mW power at the fiber tip for eOPN3 inhibition.
755      On a subset of recordings, putative ChR2-expressing units were identified by blocking excitatory
756  transmission with a mix of AMPAR and NMDAR blockers (3 mM NBQX and 6 mM APV, respectively)
757  diluted in 100 μL of recording ACSF[77]. At the end of the recording, ACSF was wicked away from the
758  recording well and the drug mixture was dripped onto the craniotomy. After at least 20 minutes (up to 45
759  minutes, based on visually-evoked responses at the deepest electrode sites) ~50 pulses of 450 nm laser
760  (10 ms, 0.1 Hz) were presented to activate ChR2-expressing cells.
761
762  *In vitro slice preparation*. Mice were deeply anesthetized with isoflurane, the brain was removed and then
763  transferred to oxygenated (95% $O_2$ and 5% $CO_2$), ice-cold artificial cerebrospinal fluid (ACSF, in mM:
764  NaCl 126, KCl 2.5, $NaHCO_3$ 26, $NaH_2PO_4$ 1.25, glucose 20, $CaCl_2$ 2, $MgCl_2$ 1.3). Coronal brain slices
765  (300 μm thickness) were prepared using a vibrating microtome (VT1200S, Leica) and transferred to a
766  holding solution (at 34º C) for 12 minutes, and then transferred to storage solution for 30 min before being
767  brought to room temperature. The holding solution contained (in mM): 92 NaCl, 2.5 KCl, 1.25 $NaH_2PO_4$,
768  30 $NaHCO_3$, 20 HEPES, 25 glucose, 2 thiourea, 5 Na-ascorbate, 3 Na-pyruvate, 2 $CaCl_2$, 2 $MgSO_4$. The
769  storage solution contained (in mM): 93 NMDG, 2.5 KCl, 1.2 $NaH_2PO_4$, 30 $NaHCO_3$, 20 HEPES, 25
770  glucose, 2 thiourea, 5 Na-ascorbate, 3 Na-pyruvate, 0.5 $CaCl_2$, 10 $MgSO_4$. Micropipettes pulled from
771  borosilicate glass (1B150F-4, World Precision Instruments) were filled with internal solution containing
772  (in mM): 142 K-gluconate, 3 KCl, 10 HEPES, 0.5 EGTA, 5 phosphocreatine-tris, 5 phosphocreatine-Na2,
773  3 Mg-ATP, 0.5 GTP. Recording pipettes had resistances of 3-5 MΩ.
774
775  *In vitro slice recordings.* Recordings occurred between 1.5 and 5 hours after the animal was sacrificed.
776  Brain slices were transferred to a recording chamber and maintained at 34º C in oxygenated ACSF
777  perfused at 2 mL/min. Electrophysiological recordings were restricted to layer 2/3 and V1 was identified
778  either by reference atlas alignment or visualization of fluorescence expression at the viral injection site.
779  Neural signals were recorded using a MultiClamp 700B and digitized with a Digidata 1550 (Axon
780  Instruments) with a 20 kHz sample rate. Data acquisition and stimulus presentation was controlled using
781  the Clampex software package (pClamp 10.5, Axon Instruments).
782      In current-clamp recordings, a constant positive current was injected to maintain membrane
783  potential near resting membrane potential measured *in vivo*. To test effects of depolarization on
784  membrane potential, positive current was injected for a duration that varied between 0.1 and 5 s. Current
785  level was calibrated with 0.1 s current injections to elicit a similar firing rate (~30 Hz) across cells, but
786  generally ranged between 400-600 pA.
787      In voltage-clamp recordings, series resistance was monitored using -5 mV steps preceding each
788  trial. At least 10 sweeps were collected for each recording condition. Only cells that had < 20 MΩ series
789  resistance, < 20% series resistance change, and stable holding current (<100 pA baseline variation) were
790  included for analysis. EPSCs were evoked by either electrical stimulation with a steel monopolar
791  electrode placed in L4 or L2/3 (100 μs pulse) or optical activation of ChR2 over cell bodies in L4 (light

792 power 0.5-1.5 mW/mm$^2$, 470 nm LED, 100 ms square pulse). For optical activation, light pulses from a
793 4-color LED controller (ThorLabs) were coupled to the epifluorescence path (Olympus BX-RFA) and
794 projected through a 40x water immersion lens (Olympus, 0.8 NA). To minimize polysynaptic activation,
795 electrical and optical stimulation intensities were calibrated to elicit EPSCs with ~100-250 pA amplitude
796 and short latency (< 5 ms).
797      Since electrical stimulation activates axons non-selectively, in a separate set of experiments in
798 Scnn1a-Cre x Ai32 animals we compared EPSCs in L2/3 neurons in response to electrical and
799 optogenetic activation in L4. After patching a L2/3 neuron, a small spot (50 μm, 100 μs) of 470 nm light
800 was used to search for an area in L4 that elicited short-latency, monosynaptic responses. The stimulation
801 electrode was placed in the center of this spot, presumably near a L4 neuron synapsing onto the L2/3
802 neuron being recorded. EPSCs recorded in L2/3 neurons displayed the same depression for electrical
803 and optogenetic stimulation, indicating that L4 electrical stimulation is sufficient to reveal the dynamics of
804 L4-L2/3 synapses (**Figure S4**).
805      eOPN3 in L4 terminals was activated by illuminating a small area (100 μm diameter) around the
806 recorded neuron with green light (0.8 mW/mm$^2$, 530 nm LED) for 10 s, followed by a 0.5 s top-up
807 preceding each trial.
808
809 *Post hoc histology*. After recording in virally injected or electroporated animals, brains were imaged to
810 confirm viral expression in the recorded area. For *in vitro* recordings, slices were incubated 12-16 hours
811 in 4% paraformaldehyde (PFA) in PBS, washed 3x with PBS and mounted. For *in vivo* recordings, the
812 probe tract was visualized with DiI or DiO painted on the probe prior to insertion (Invitrogen V22889).
813 After recording, animals were anesthetized with an overdose of ketamine/xylazine and perfused with PBS
814 followed by 4% PFA in PBS. Brains were dissected and incubated in 4% PFA overnight, rinsed 3x with
815 PBS, then sliced in 100 μm sections and mounted on glass slides. Slides were mounted with Fluoromount
816 G with DAPI (Invitrogen) and imaged using a Zeiss inverted microscope (Zeiss Axiovert).
817
818 **QUANTIFICATION AND STATISTICAL ANALYSIS**
819
820 All analyses were performed in custom code written in either MATLAB or Python. All data are presented
821 as mean ± SEM. N values refer to number of cells or units isolated. Sample sizes were not predetermined
822 but are comparable to published literature for each type of experiment. For all experiments adaptation is
823 quantified as the normalized response:

824
$$Norm.Response = \frac{Test}{Baseline}$$

825
826 Where the *Baseline* response is the response to the first visual stimulus (or electrical or optical stimulus
827 *in vitro)* on a trial and the *Test* is the response to the same stimulus following a visual, electrical, or optical
828 adapter.
829
830 Analysis of *in vivo* whole-cell recordings
831
832 *Current clamp recordings.* Raw membrane potential was separated into firing rate and subthreshold
833 membrane potential. Firing rate was obtained by setting a voltage threshold on a cell-by-cell basis for
834 detecting spikes. Subthreshold membrane potential was obtained by using a median filter to clip spikes.
835 For each ISI, pre-stimulus mean membrane potential and variance were measured from subthreshold
836 membrane potential in a 0.1 s window prior to stimulus onset. Spike threshold was measured from spikes
837 detected in a 0.4 s window around stimulus onset (0.1 s before and 0.3 s after stimulus onset). Spike
838 threshold was calculated by averaging over the membrane potential at the time of the peak of the second
839 derivative for all spikes within this time window. PSP amplitude was measured in a 20 ms window around
840 the peak of the trial-averaged response during the stimulus-evoked response window (0-0.25 s after
841 stimulus onset), relative to the baseline window (0.1 s before stimulus onset).

842

843    *Voltage clamp recordings.* EPSC or IPSC stimulus-evoked amplitude was quantified by averaging current
844    values within a 20 ms window around the peak of the response in the stimulus-evoked response window
845    (0-0.25 s after stimulus onset). Mean and standard deviation of the holding current was quantified in a
846    0.1 s window prior to stimulus onset. Recovery time constants were fit for EPSCs and IPSCs using a
847    single exponential from the normalized current amplitude averaged across cells. For all stimulus
848    specificity experiments, current amplitudes were normalized to the baseline stimulus of the same
849    orientation. Adaptation tuning width was measured by fitting the normalized responses with a von Mises
850    function.

851

852    Analysis of *in vitro* whole-cell recordings

853

854    Amplitudes of EPSCs in response to electrical stimulation or 0.01 s ChR2 activation were calculated as
855    the mean of the trial-averaged response in a 2 ms window around the peak of the response. Amplitudes
856    of EPSCs in response to 0.1 s ChR2 activation were calculated in a 20 ms window around the peak of
857    the response. Recovery of optogenetically evoked EPSCs from adaptation with 0.1 s ChR2 activation
858    was fit with a single exponential.

859

860    Analysis of extracellular recordings

861

862    *Spike sorting.* Single units were isolated with KiloSort 2.5 (https://github.com/MouseLand/Kilosort) using
863    refractory period violations and steepness of the autocorrelogram as criteria for isolation. We then
864    manually curated these units in Phy (https://github.com/cortex-lab/phy) such that only units that were
865    detected throughout the entire recording are included for subsequent analysis. Depth of the unit was
866    assigned based on their waveforms' center-of-mass across sites. Fast-spiking (FS) and regular-spiking
867    (RS) units were separated within recordings according to peak-to-trough time of the maximum amplitude
868    waveform across all contact sites (**Figure S3**).

869

870    *Layer identification.* To functionally identify cortical layers, we used the local field potential (LFP) obtained
871    from filtering the raw data (downsampled to 10 kHz) from 1 to 200 Hz. The trial-averaged, stimulus-
872    evoked LFP during a 1-second drifting grating presentation was converted to a current source density
873    (CSD) plot by taking the discrete second derivative across the electrode sites and interpolated. Layer
874    bounds were assigned relative to an initial sink in layer 4, followed by a sink in layer 2/3 and a sustained
875    sink in layer 5 (**Figure S5**).
876            To confirm layer identification, in a subset of experiments ChR2-activated units were identified in
877    the presence of excitatory synaptic blockers to identify ChR2-expressing units. Each unit's distance in
878    depth from the L23-L4 boundary was measured to compare depth of L4 versus L2/3 ChR2-expressing
879    neurons across the two experiment types (**Figure S5**).

880

881    *Data inclusion and analysis.* For all recordings, only cells that were visually responsive, according to a
882    paired t-test in a 0.15 s window before and after stimulus onset, were included. In ChR2 activation
883    experiments, "laser active" units were defined as units significantly driven by ChR2 activation in this same
884    time window. For eOPN experiments, inhibited and facilitated units were defined as having >20%
885    decrease or increase, respectively, in visually-evoked responses during eOPN3 activation compared to
886    control trials. Categorization of units with significant increase or decrease defined by paired t-test yielded
887    similar results. Neurons that were classified as inhibited in L2/3 and L4 were monitored for recovery of
888    visually-evoked responses following eOPN3 activation and the recovery time constant was fit with a
889    single exponential from the start of eOPN3 induction.
890            PSTHs were generated by binning spiking activity in 0.01 s windows across all trials of each type,
891    aligned to stimulus onset. Each stimulus condition contained at least 20 repeats. Maximum firing rate
892    was measured as the average firing rate in a 20 ms window around the peak of the PSTH. For plots

893  visualizing average stimulus-evoked responses across units, firing rates were z-scored prior to averaging.
894  Orientation tuning was measured using the mean firing rate in a 20 ms window around the peak PSTH
895  for each stimulus direction, collapsed by orientation and fit with a von Mises function.
896
897  **Supplemental Figures**
898
899  **Figure S1. Rapid adaptation does not induce cell-intrinsic fatigue, related to Figure 1. A.** Histogram
900  of single trial correlation of spikes elicited in response to baseline and test stimuli for 0.25 ISI condition
901  from intracellular (left; n = 13 cells) and extracellular (right; n = 43 units) L2/3 *in vivo* recordings. Dark
902  gray bars indicate significant correlations. **B.** Current clamp recording in example L2/3 pyramidal cell in
903  response to current injections of two durations (black = 0.1 s, gray = 1 s). **C.** Change in membrane
904  potential (Vm) following offset of increasing current injection durations in the example cell in **B**. **D.**
905  Average change in membrane potential after current injection offset at recovery times when spike output
906  is suppressed (0.25 s) or recovered (4 s) *in vivo* for increasing current durations. Dashed line is average
907  change in stimulus-evoked membrane potential *in vivo*. Error bar is SEM across cells.
908
909  **Figure S2. Whole-cell voltage clamp recording of EPSCs and IPSCs *in vivo*, related to Figure 2.**
910  **A.** Reversal potential of currents evoked with optogenetic activation of parvalbumin-expressing (PV)
911  interneurons expressing Channelrhodopsin-2 (ChR2) to calibrate reversal potential for inhibitory currents
912  in vivo (PV-Cre mice injected with AAV2/1.hSyn.ChR2-YFP; n = 4 cells). **B.** Series resistance (Rs) during
913  recording of EPSCs (black) and IPSCs (red). Thick lines are average across cells. Dashed line is cutoff
914  used for series resistance inclusion criteria. **C.** Normalized current (baseline/test; 0.25 s ISI) as a function
915  of series resistance for all recordings. Grey arrows connect currents recorded within the same cell and
916  direction reflects the order of recording. P-value is significance of Pearson correlation.
917
918  **Figure S3. Separation of FS and RS units and comparison of orientation tuning, related to Figures**
919  **2 and 3. A.** Peak-trough time of spike waveforms from units classified as regular spiking (RS, black) or
920  fast spiking (FS, grey). **B.** Average spike waveforms from the units in **A**. Shaded error is SEM across
921  units. **C.** Average orientation tuning curves aligned to preferred orientation for each unit. Points are
922  averaged normalized response across units. Curves are averages of the von Mises fit for individual units.
923
924  **Figure S4. EPSCs in L2/3 measured with ChR2 and electrical stimulation, related to Figure 4. A.**
925  Schematic of recording EPSCs from a L2/3 pyramidal cell while stimulating L4 neurons optogenetically
926  or electrically on alternating trials. **B.** Average EPSCs from an example cell in response to optogenetic
927  (blue) or electrical (black) stimulation of L4 for the first (dark) and last (light) stimulus in the train. **C.**
928  Average EPSC amplitude normalized to first pulse within stimulation type. Error bar is SEM across cells.
929  Two-way ANOVA, p = 0.51 for effect of stimulation type.
930
931  **Figure S5. Identification of layer boundaries for classifying units as L2/3 or L4, related to Figures**
932  **5, 6 and 8. A.** Local field potential (LFP) measured across cortical depths during a drifting grating stimulus
933  from an example recording. Traces are colored according to contact site from superficial (red) to deep
934  (black). **B.** Current source density (CSD) calculated using the LFP in **A**. Dashed lines indicate layer
935  boundaries assigned based on this map. L4 was assigned by identifying an early onset sink and L2/3
936  was identified as the later onset sink above it. **C.** Example units identified as ChR2+ (left) or ChR2- (right).
937  PSTH and spike rasters in response to blue laser pulses (10 ms) before (top) and after (bottom)

pharmacological block of excitatory transmission (**STAR Methods**). **D.** Depth of ChR2-expressing units relative to L2/3-L4 boundary identified using the CSD. Marker fill indicates ChR2 expression layer (unfilled = L2/3, *in utero* electroporated mice; filled = L4, Scnn1a x Ai32 mice; depth of L2/3 vs L4 expression: p < 0.001, un-paired t-test).

**Figure S6. Effects of optogenetic activation of L4 neurons, related to Figure 5. A.** Average PSTH of laser active L2/3 units during optogenetic activation of L4 neurons with 5, 0.1 s square pulses of blue light. **B.** Same as A, for L4 units. **C.** Peak firing rate for each stimulus pulse, normalized to the first pulse in the train for L2/3 (black) and L4 (grey) units. Error bar is SEM across units. L2/3 p < 0.001 for stimulus 2-5 vs 1, one-way ANOVA with post hoc Tukey test. **D.** Optogenetic adaptation measured in L2/3 and L4 units across different laser durations (L4 vs L2/3, 0.5 s laser duration: p = 0.006; 1 s laser duration: p = 0.009, unpaired t-tests). Shaded box indicates laser duration used for main figure experiments. **E.** Visual adaptation measured in L2/3 neurons following different durations of optogenetic activation of L4 neurons. Dashed line is visual adaptation in the absence of L4 stimulation. **F.** Change in spontaneous firing rate after different durations of L4 activation. Dashed line is spontaneous firing rate after visual adaptation. **G.** L2/3 optogenetic adaptation in units divided by units that were significantly modulated by L4 ChR2 stimulation (solid line) or not (dashed line). **H.** Same as **G**, for L4 units.

**Figure S7. Green laser alone does not affect firing rates, related to Figure 8. A.** Average time course of stimulus-evoked, z-scored firing rate aligned to eOPN3 activation for all units recorded in L2/3 (n = 105). Green vertical lines indicate eOPN3 activation trials. Black curve is fit to the recovery from eOPN3 activation. Shaded error is SEM across units. **B.** Comparison of normalized response (test/baseline) in control and eOPN3 activation trials, for all L4 units colored by categorization in **Figure 8E** (dark green = inhibited, medium green = stable, light green = facilitated). **C.** Average normalized response for inhibited (dark green) and stable (light green) units in L4. Error bar is SEM across units. **D.** Average visually-evoked firing rate of L2/3 neurons during control and laser stimulation trials in eOPN3 (left, green) or RFP control (right, black) recordings. Individual lines are average response of all L2/3 neurons in each session, thick line is mean across sessions (eOPN: paired t-test, p < 0.001; RFP: paired t-test p = 0.39). **E.** Left: Fraction of L2/3 units classified as inhibited from recordings with eOPN3 (green) or RFP control (black) in L4 neurons. Right: Same as left, for L4 units.

**Figure S8. Effect of low contrast baseline stimulus on adaptation in L2/3, related to Figure 8. A.** Schematic of visual stimulus. Baseline stimulus was either low (40%) or high (80%) contrast and test stimulus was always high contrast. **B.** Left: Z-scored PSTH of L2/3 units during high contrast (black) or low contrast (gray) baseline visual stimulus presentation. Right: Fractional change in peak firing rate during baseline stimulus for high versus low contrast. **C.** Z-scored PSTH during test visual stimulus presentation with baseline high (black) or low contrast (gray). **D.** Average normalized firing rate (test/baseline) with high or low contrast baseline stimulus. Test responses for both trial types was divided by the baseline response to high contrast (two-way ANOVA, effect of contrast, p = 0.45).

## References

1.  Weber, A.I., Krishnamurthy, K., and Fairhall, A.L. (2019). Coding Principles in Adaptation. Annu. Rev. Vis. Sci. *5*, 427–449. 10.1146/annurev-vision-091718-014818.
2.  Barlow, H.B.H. (1961). Possible principles underlying the transformation of sensory messages. In

983      Sensory Communication, pp. 217–234. 10.1080/15459620490885644.

984  3.   Kohn, A. (2007). Visual adaptation: Physiology, mechanisms, and functional benefits. J.
985      Neurophysiol. *97*, 3155–3164. 10.1152/jn.00086.2007.

986  4.   Vinje, W.E., and Gallant, J.L. (2000). Natural Vision Sparse Coding and Decorrelation in Primary
987      Visual Cortex During Sparse Coding and Decorrelation in Primary Visual Cortex During Natural
988      Vision. Science (80-. ). *287*, 1273–1276. 10.1126/science.287.5456.1273.

989  5.   Simoncelli, E.P., and Olshausen, B.A. (2001). Natural Image Statistics and Neural
990      Representation. Annu. Rev. Neurosci. *24*, 1193–1216. 10.1146/annurev.neuro.24.1.1193.

991  6.   Schwartz, O., Hsu, A., and Dayan, P. (2007). Space and time in visual context. Nat. Rev.
992      Neurosci. *8*, 522–535. 10.1038/nrn2155.

993  7.   Parker, P.R.L., Abe, E.T.T., Leonard, E.S.P., Martins, D.M., and Niell, C.M. (2022). Joint coding
994      of visual input and eye/head position in V1 of freely moving mice. Neuron, 1–10.
995      10.1016/j.neuron.2022.08.029.

996  8.   Nigam, S., Milton, R., Pojoga, S., and Dragoi, V. (2023). Adaptive coding across visual features
997      during free-viewing and fixation conditions. Nat. Commun. *14*, 87. 10.1038/s41467-022-35656-w.

998  9.   Latimer, K.W., Barbera, D., Sokoletsky, M., Awwad, B., Katz, Y., Nelken, I., Lampl, I., Fairhall,
999      A.L., and Priebe, N.J. (2019). Multiple timescales account for adaptive responses across sensory
1000      cortices. J. Neurosci. *39*, 10019–10033. 10.1523/JNEUROSCI.1642-19.2019.

1001  10.   Ulanovsky, N., Las, L., Farkas, D., and Nelken, I. (2004). Multiple time scales of adaptation in
1002      auditory cortex neurons. J. Neurosci. *24*, 10440–10453. 10.1523/JNEUROSCI.1905-04.2004.

1003  11.   Zucker, R.S., and Regehr, W.G. (2002). Short-term synaptic plasticity. Annu. Rev. Physiol. *64*,
1004      355–405. 10.1146/annurev.physiol.64.092501.114547.

1005  12.   Varela, J.A., Sen, K., Gibson, J., Fost, J., Abbott, L.F., and Nelson, S.B. (1997). A quantitative
1006      description of short-term plasticity at excitatory synapses in layer 2/3 of rat primary visual cortex.
1007      J. Neurosci. *17*, 7926–7940.

1008  13.   Abolafia, J.M., Vergara, R., Arnold, M.M., Reig, R., and Sanchez-Vives, M. V. (2011). Cortical
1009      auditory adaptation in the awake rat and the role of potassium currents. Cereb. Cortex *21*, 977–
1010      990. 10.1093/cercor/bhq163.

1011  14.   Beck, O., Chistiakova, M., Obermayer, K., and Volgushev, M. (2005). Adaptation at synaptic
1012      connections to layer 2/3 pyramidal cells in rat visual cortex. J. Neurophysiol. *94*, 363–376.
1013      10.1152/jn.01287.2004.

1014  15.   Baccus, S.A., and Meister, M. (2002). Fast and slow contrast adaptation in retinal circuitry.
1015      Neuron *36*, 909–919. 10.1016/S0896-6273(02)01050-4.

1016  16.   Patterson, C.A., Wissig, S.C., and Kohn, A. (2013). Distinct Effects of Brief and Prolonged
1017      Adaptation on Orientation Tuning in Primary Visual Cortex. J. Neurosci. *33*, 532–543.
1018      10.1523/JNEUROSCI.3345-12.2013.

1019  17.   Wolfe, J.M. (1984). Short test flashes produce large tilt aftereffects. Vision Res. *24*, 1959–1964.
1020      10.1016/0042-6989(84)90030-0.

1021  18.   Harris, J.P., and Calvert, J.E. (1989). Contrast, spatial frequency and test duration effects on the
1022      tilt aftereffect: Implications for underlying mechanisms. Vision Res. *29*, 129–135. 10.1016/0042-
1023      6989(89)90179-X.

1024  19.   Jin, M., Beck, J.M., and Glickfeld, L.L. (2019). Neuronal adaptation reveals a suboptimal
1025      decoding of orientation tuned populations in the mouse visual cortex. J. Neurosci., 3172–18.
1026      10.1523/JNEUROSCI.3172-18.2019.

1027  20.   Jin, M., and Glickfeld, L.L. (2020). Magnitude, time course, and specificity of rapid adaptation
1028      across mouse visual areas. J. Neurophysiol. *124*, 245–258. 10.1152/jn.00758.2019.

1029  21.   Fritsche, M., Solomon, S.G., and de Lange, F.P. (2022). Brief Stimuli Cast a Persistent Long-
1030      Term Trace in Visual Cortex. J. Neurosci. *42*, 1999–2010. 10.1523/jneurosci.1350-21.2021.

1031  22.   Sanchez-Vives, M. V, Nowak, L.G., and McCormick, D.A. (2000). Membrane mechanisms
1032      underlying contrast adaptation in cat area 17 in vivo. J Neurosci *20*, 4267–4285. 20/11/4267 [pii].

1033  23.   Carandini, M., and Ferster, D. (1997). A Tonic Hyperpolarization Underlying Contrast A Tonic

Hyperpolarization Underlying Contrast Adaptation in Cat Visual Cortex. *276*, 949–952. 10.1126/science.276.5314.949.

24.  Wehr, M., and Zador, A.M. (2005). Synaptic mechanisms of forward suppression in rat auditory cortex. Neuron *47*, 437–445. 10.1016/j.neuron.2005.06.009.

25.  Chung, S., Li, X., and Nelson, S.B. (2002). Short-term depression at thalamocortical synapses contributes to rapid adaptation of cortical sensory responses in vivo. Neuron *34*, 437–446. 10.1016/S0896-6273(02)00659-1.

26.  Natan, R.G., Briguglio, J.J., Mwilambwe-Tshilobo, L., Jones, S.I., Aizenberg, M., Goldberg, E.M., and Geffen, M.N. (2015). Complementary control of sensory adaptation by two types of cortical interneurons. Elife *4*, 1–27. 10.7554/elife.09868.

27.  Boudreau, C.E., and Ferster, D. (2005). Short-term depression in thalamocortical synapses of cat primary visual cortex. J. Neurosci. *25*, 7179–7190. 10.1523/JNEUROSCI.1445-05.2005.

28.  Hu, B., Garrett, M.E., Groblewski, P.A., Ollerenshaw, D.R., Shang, J., Roll, K., Manavi, S., Koch, C., Olsen, S.R., and Mihalas, S. (2021). Adaptation supports short-term memory in a visual change detection task. PLoS Comput. Biol. *17*, 1–22. 10.1371/journal.pcbi.1009246.

29.  Sohya, K., Kameyama, K., Yanagawa, Y., Obata, K., and Tsumoto, T. (2007). GABAergic neurons are less selective to stimulus orientation than excitatory neurons in layer II/III of visual cortex, as revealed by in vivo functional Ca2+ imaging in transgenic mice. J. Neurosci. *27*, 2145–2149. 10.1523/JNEUROSCI.4641-06.2007.

30.  Niell, C., and Stryker, M. (2008). Highly Selective Receptive Fields in Mouse Visual Cortex. J. Neurosci. *28*, 7520–7536. 10.1523/JNEUROSCI.0623-08.2008.

31.  Kerlin, A.M., Andermann, M.L., Berezovskii, V.K., and Reid, R.C. (2010). Broadly Tuned Response Properties of Diverse Inhibitory Neuron Subtypes in Mouse Visual Cortex. Neuron *67*, 858–871. 10.1016/j.neuron.2010.08.002.

32.  Hage, T.A., Bosma-Moody, A., Baker, C.A., Kratz, M.B., Campagnola, L., Jarsky, T., Zeng, H., and Murphy, G.J. (2022). Synaptic connectivity to L2/3 of primary visual cortex measured by two-photon optogenetic stimulation. Elife *11*, 1–46. 10.7554/elife.71103.

33.  Lefort, S., and Petersen, C.C.H. (2017). Layer-Dependent Short-Term Synaptic Plasticity between Excitatory Neurons in the C2 Barrel Column of Mouse Primary Somatosensory Cortex. Cereb. Cortex *27*, 3869–3878. 10.1093/cercor/bhx094.

34.  Mahn, M., Saraf-Sinik, I., Patil, P., Pulin, M., Bitton, E., Karalis, N., Bruentgens, F., Palgi, S., Gat, A., Dine, J., et al. (2021). Efficient optogenetic silencing of neurotransmitter release with a mosquito rhodopsin. Neuron *109*, 1621-1635.e8. 10.1016/j.neuron.2021.03.013.

35.  Chance, F.S., Nelson, S.B., and Abbott, L.F. (1998). Synaptic depression and the temporal response characteristics of V1 cells. J. Neurosci. *18*, 4785–4799.

36.  Abbott, L.F., Varela, J.A., Sen, K., and Nelson, S.B. (1997). Synaptic depression and cortical gain control. Science (80-. ). *275*, 220–224. 10.1126/science.275.5297.221.

37.  Feldmeyer, D., Lübke, J., Silver, R.A., and Sakmann, B. (2002). Synaptic connections between layer 4 spiny neurone-layer 2/3 pyramidal cell pairs in juvenile rat barrel cortex: Physiology and anatomy of interlaminar signalling within a cortical column. J. Physiol. *538*, 803–822. 10.1113/jphysiol.2001.012959.

38.  Higley, M.J. (2006). Balanced Excitation and Inhibition Determine Spike Timing during Frequency Adaptation. J. Neurosci. *26*, 448–457. 10.1523/JNEUROSCI.3506-05.2006.

39.  Whitmire, C.J., and Stanley, G.B. (2016). Rapid Sensory Adaptation Redux: A Circuit Perspective. Neuron *92*, 298–315. 10.1016/j.neuron.2016.09.046.

40.  Heiss, J.E., Katz, Y., Ganmor, E., and Lampl, I. (2008). Shift in the balance between excitation and inhibition during sensory adaptation of S1 neurons. J. Neurosci. *28*, 13320–13330. 10.1523/JNEUROSCI.2646-08.2008.

41.  Carandini, M., Heeger, D.J., and Senn, W. (2002). A synaptic explanation of suppression in visual cortex. J. Neurosci. *22*, 10053–10065. 10.1523/jneurosci.22-22-10053.2002.

42.  Gabernet, L., Jadhav, S.P., Feldman, D.E., Carandini, M., and Scanziani, M. (2005).

1085   Somatosensory integration controlled by dynamic thalamocortical feed-forward inhibition. Neuron
1086   *48*, 315–327. 10.1016/j.neuron.2005.09.022.

1087 43. Crowder, N.A., Price, N.S.C., Hietanen, M.A., Dreher, B., Clifford, C.W.G., and Ibbotson, M.R.
1088   (2006). Relationship between contrast adaptation and orientation tuning in V1 and V2 of cat
1089   visual cortex. J. Neurophysiol. *95*, 271–283. 10.1152/jn.00871.2005.

1090 44. Borst, J.G.G. (2010). The low synaptic release probability in vivo. Trends Neurosci. *33*, 259–266.
1091   10.1016/j.tins.2010.03.003.

1092 45. Chen, C., and Regehr, W.G. (2003). Presynaptic modulation of the retinogeniculate synapse. J.
1093   Neurosci. *23*, 3130–3135. 10.1523/jneurosci.23-08-03130.2003.

1094 46. Stratford, K.J., Tarczy-Hornoch, K., Martin, K.A.C., Bannister, N.J., and Jack, J.J.B. (1996).
1095   Excitatory synaptic inputs to spiny stellate cells in cat visual cortex. Nature *382*, 258–261.
1096   10.1038/382258a0.

1097 47. Gil, Z., Connors, B.W., and Amitai, Y. (1997). Differential regulation of neocortical synapses by
1098   neuromodulators and activity. Neuron *19*, 679–686. 10.1016/S0896-6273(00)80380-3.

1099 48. Litvina, E.Y., and Chen, C. (2017). An evolving view of retinogeniculate transmission. Vis.
1100   Neurosci. *34*. 10.1017/S0952523817000104.

1101 49. Hirsch, J.A., Martinez, L.M., Alonso, J.M., Desai, K., Pillai, C., and Pierre, C. (2002). Synaptic
1102   physiology of the flow of information in the cat's visual cortex in vivo. J. Physiol. *540*, 335–350.
1103   10.1113/jphysiol.2001.012777.

1104 50. Nelson, S.B., and Turrigiano, G.G. (1998). Synaptic depression: A key player in the cortical
1105   balancing act. Nat. Neurosci. *1*, 539–541. 10.1038/2775.

1106 51. Seay, M.J., Natan, R.G., Geffen, M.N., and Buonomano, D. V. (2020). Differential short-term
1107   plasticity of PV and SST neurons accounts for adaptation and facilitation of cortical neurons to
1108   auditory tones. J. Neurosci. *40*, 9224–9235. 10.1523/JNEUROSCI.0686-20.2020.

1109 52. Hu, H., and Agmon, A. (2016). Differential excitation of distally versus proximally targeting
1110   cortical interneurons by unitary thalamocortical bursts. J. Neurosci. *36*, 6906–6916.
1111   10.1523/JNEUROSCI.0739-16.2016.

1112 53. Wright, N.C., Borden, P.Y., Liew, Y.J., Bolus, M.F., Stoy, W.M., Forest, C.R., and Stanley, G.B.
1113   (2021). Rapid Cortical Adaptation and the Role of Thalamic Synchrony during Wakefulness. J.
1114   Neurosci. *41*, 5421–5439. 10.1523/JNEUROSCI.3018-20.2021.

1115 54. Yarden, T.S., Mizrahi, A., and Nelken, I. (2022). Context-Dependent Inhibitory Control of
1116   Stimulus-Specific Adaptation Context-Dependent Inhibitory Control of Stimulus-Specific
1117   Adaptation Abbreviated Title: 4 Inhibitory Control of Stimulus-Specific Adaptation. *42*, 4629–
1118   4651.

1119 55. Yavorska, I., and Wehr, M. (2016). Somatostatin-expressing inhibitory interneurons in cortical
1120   circuits. Front. Neural Circuits *10*, 1–18. 10.3389/fncir.2016.00076.

1121 56. Beierlein, M., Gibson, J.R., and Connors, B.W. (2003). Two Dynamically Distinct Inhibitory
1122   Networks in Layer 4 of the Neocortex. J. Neurophysiol. *90*, 2987–3000. 10.1152/jn.00283.2003.

1123 57. Heintz, T.G., Hinojosa, A.J., Dominiak, S.E., and Lagnado, L. (2022). Opposite forms of
1124   adaptation in mouse visual cortex are controlled by distinct inhibitory microcircuits. Nat.
1125   Commun. *13*, 1–14. 10.1038/s41467-022-28635-8.

1126 58. Phillips, E.A.K., Schreiner, C.E., and Hasenstaub, A.R. (2017). Cortical Interneurons
1127   Differentially Regulate the Effects of Acoustic Context. Cell Rep. *20*, 771–778.
1128   10.1016/j.celrep.2017.07.001.

1129 59. Hamm, J.P., and Yuste, R. (2016). Somatostatin Interneurons Control a Key Component of
1130   Mismatch Negativity in Mouse Visual Cortex. Cell Rep. *16*, 597–604.
1131   10.1016/j.celrep.2016.06.037.

1132 60. Varela, J.A., Song, S., Turrigiano, G.G., and Nelson, S.B. (1999). Differential depression at
1133   excitatory and inhibitory synapses in visual cortex. J. Neurosci. *19*, 4293–4304.
1134   10.1523/jneurosci.19-11-04293.1999.

1135 61. Kapfer, C., Glickfeld, L.L., Atallah, B. V, and Scanziani, M. (2007). Supralinear increase of

recurrent inhibition during sparse activity in the somatosensory cortex. Nat. Neurosci. *10*, 743–753. 10.1016/j.immuni.2010.12.017.Two-stage.

62. Reyes, A., Lujan, R., Rozov, A., Burnashev, N., Somogyi, P., and Sakmann, B. (1998). Target-cell-specific facilitation and depression in neocortical circuits. Nat. Neurosci. *1*, 279–284. 10.1038/1092.

63. Pala, A., and Petersen, C.C.H. (2015). InVivo Measurement of Cell-Type-Specific Synaptic Connectivity and Synaptic Transmission in Layer 2/3 Mouse Barrel Cortex. Neuron *85*, 68–75. 10.1016/j.neuron.2014.11.025.

64. Scholl, B., Thomas, C.I., Ryan, M.A., Kamasawa, N., and Fitzpatrick, D. (2020). Cortical response selectivity derives from strength in numbers of synapses. Nature *12*. 10.1038/s41586-020-03044-3.

65. Petersen, C.C.H., and Crochet, S. (2013). Synaptic Computation and Sensory Processing in Neocortical Layer 2/3. Neuron *78*, 28–48. 10.1016/j.neuron.2013.03.020.

66. Tsodyks, M. V., and Markram, H. (1997). The neural code between neocortical pyramidal neurons depends on neurotransmitter release probability. Proc. Natl. Acad. Sci. U. S. A. *94*, 719–723. 10.1073/pnas.94.2.719.

67. Chance, F.S., and Abbott, L.F. (2001). Input-specific adaptation in complex cells through synaptic depression. Neurocomputing *38–40*, 141–146. 10.1016/S0925-2312(01)00550-1.

68. Foley, J.M., and Boynton, G.M. (1993). Forward pattern masking and adaptation: Effects of duration, interstimulus interval, contrast, and spatial and temporal frequency. Vision Res. *33*, 959–980. 10.1016/0042-6989(93)90079-C.

69. Nagel, K.I., Hong, E.J., and Wilson, R.I. (2015). Synaptic and circuit mechanisms promoting broadband transmission of olfactory stimulus dynamics. Nat. Neurosci. *18*, 56–65. 10.1038/nn.3895.

70. Horwitz, G.D. (2020). Temporal information loss in the macaque early visual system 10.1371/journal.pbio.3000570.

71. Reinhold, K., Lien, A.D., and Scanziani, M. (2015). Distinct recurrent versus afferent dynamics in cortical visual processing. Nat. Neurosci. *18*, 1789–1797. 10.1038/nn.4153.

72. Douglas, R.J., and Martin, K.A.C. (2004). Neuronal Circuits of the Neocortex. Annu. Rev. Neurosci. *27*, 419–451. 10.1146/annurev.neuro.27.070203.144152.

73. Cheetham, C.E.J., and Fox, K. (2010). Presynaptic development at L4 to L2/3 excitatory synapses follows different time courses in visual and somatosensory cortex. J. Neurosci. *30*, 12566–12571. 10.1523/JNEUROSCI.2544-10.2010.

74. Voelcker, B., Pancholi, R., and Peron, S. (2022). Transformation of primary sensory cortical representations from layer 4 to layer 2. Nat. Commun. *13*, 5484. 10.1038/s41467-022-33249-1.

75. Castro-Alamancos, M.A. (2004). Absence of Rapid Sensory Adaptation in Neocortex during Information Processing States. Neuron *41*, 455–464. 10.1016/S0896-6273(03)00853-5.

76. Edelstein, A.D., Tsuchida, M.A., Amodaj, N., Pinkard, H., Vale, R.D., and Stuurman, N. (2014). Advanced methods of microscope control using µManager software. J. Biol. Methods *1*, e10. 10.14440/jbm.2014.36.

77. Sanzeni, A., Akitake, B., Goldbach, H.C., Leedy, C.E., Brunel, N., and Histed, M.H. (2020). Inhibition stabilization is a widespread property of cortical networks. Elife *9*, 1–39. 10.7554/eLife.54875.

## Figure 1



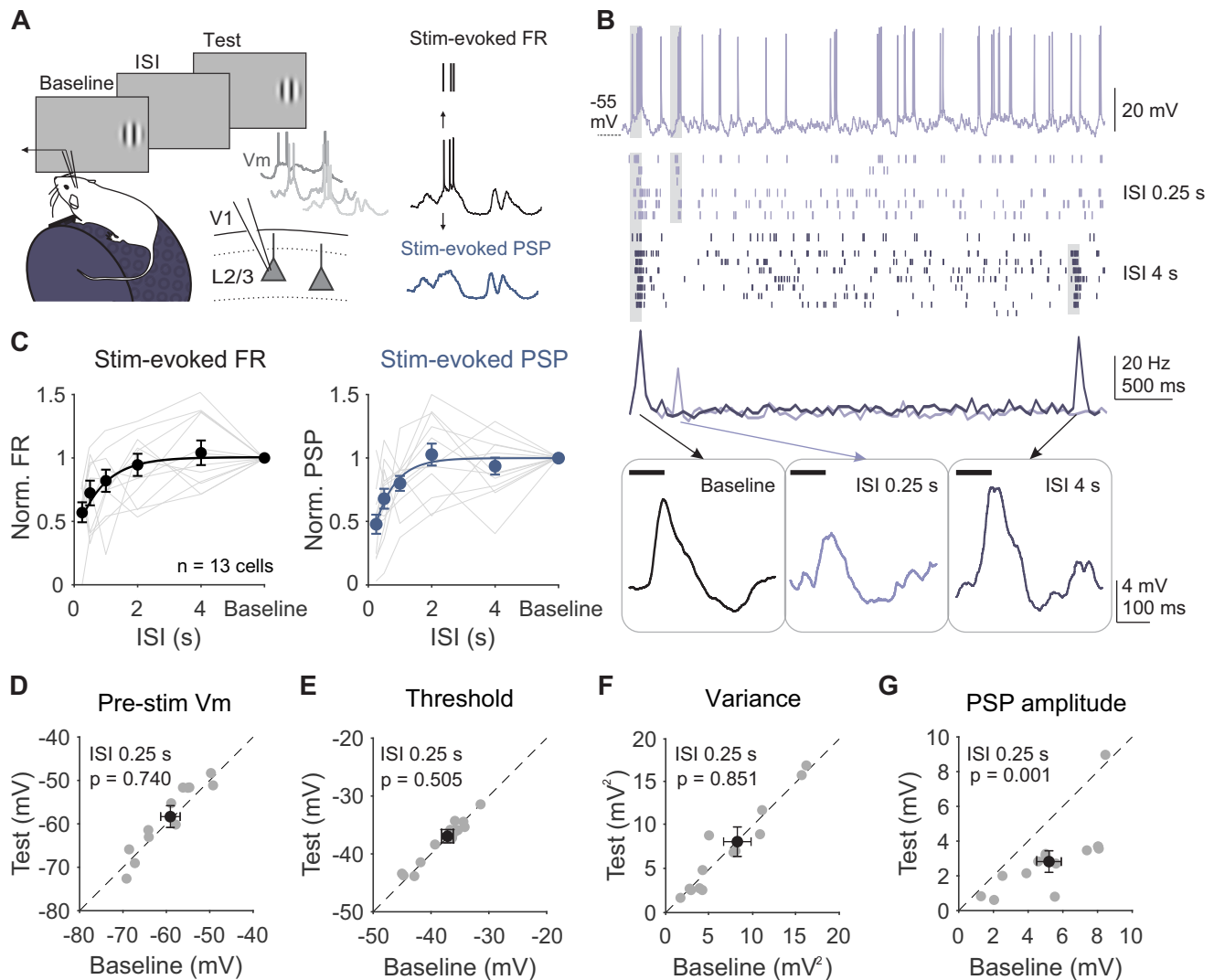**Figure 1. Adaptation suppresses stimulus-evoked responses in L2/3 neurons without affecting cell-intrinsic properties. A.** Left: Recording setup and stimulus paradigm. Animals are head-fixed on a treadmill and membrane potential (Vm) of L2/3 neurons is recorded with a glass pipette. Two stimuli (baseline and test; 0.1 s) are separated by an inter-stimulus interval (ISI) varying from 0.25 to 4 s. Right: Membrane potential is separated into the stimulus-evoked firing rate (black) and stimulus-evoked post-synaptic potential (blue; PSP). **B.** Top: Membrane potential from an example cell during a 0.25 s ISI trial. Grey shading indicates stimulus presentation. Middle: Raster plot of spike output during 0.25 s (light purple) and 4 s (dark purple) ISI trials and binned peri-stimulus spike histogram (PSTH). Bottom: Subthreshold membrane potential during baseline (left) and test stimulus presentations at 0.25 s (middle) and 4 s (right) ISIs. **C.** Left: Average normalized firing rate (FR; test/baseline) as a function of ISI for individual cells (gray lines) and all cells (black circles; n = 13). Error is SEM across cells. Black line is an exponential fit ($\tau = 0.82$ s). Right: Same as left, for average normalized PSP amplitude ($\tau = 0.79$ s). **D.** Average membrane potential preceding baseline and test stimuli for individual cells in 0.25 s ISI trials. Black dot is mean across cells. Error bar is SEM across cells. **E-G.** Same as **D** for spike threshold (**E**), membrane variance (**F**), and PSP amplitude (**G**).

## Figure 2
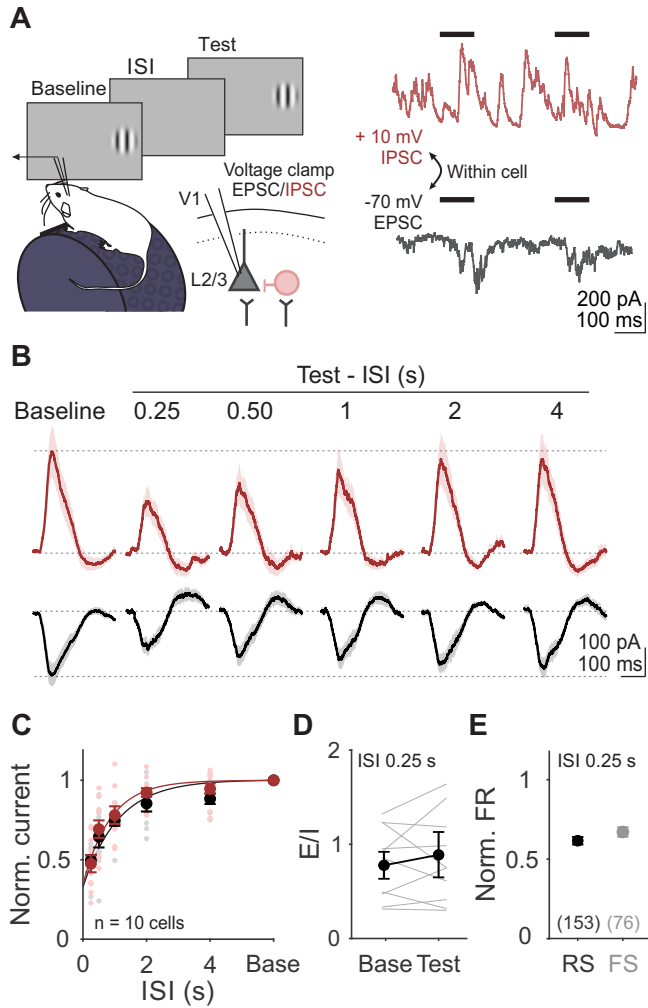


**Figure 2. Adaptation drives a balanced reduction in stimulus-evoked excitation and inhibition. A.** Left: Schematic of recording setup for measuring excitatory and inhibitory currents (EPSCs and IPSCs) in L2/3 neurons. Right: Single trial voltage traces from an example cell held at - 70 mV (black) and +10 mV (red), to measure EPSCs and IPSCs respectively. **B.** Grand average of stimulus-evoked EPSCs and IPSCs across all cells (n = 10) in response to baseline and test stimuli for all ISIs. Shaded error is SEM across cells. **C.** Average normalized current amplitudes (test/baseline) for EPSCs (black) and IPSCs (red) for individual cells (small dots) and across all cells (large dots). Curve is exponential fit to the average across cells for each current type. Error bar is SEM across cells. **D.** Ratio of excitation to inhibition (E/I) for the baseline and test stimulus in 0.25 s ISI trials. Grey lines are individual cells, black line is average across cells, error is SEM across cells. **E.** Comparison of visual adaptation in 0.25 s ISI trials in putative pyramidal cells (RS, black) and inhibitory interneurons (FS, gray), obtained from extracellular recordings (**Figure S3**). Error bar is SEM across units.

## Figure 3
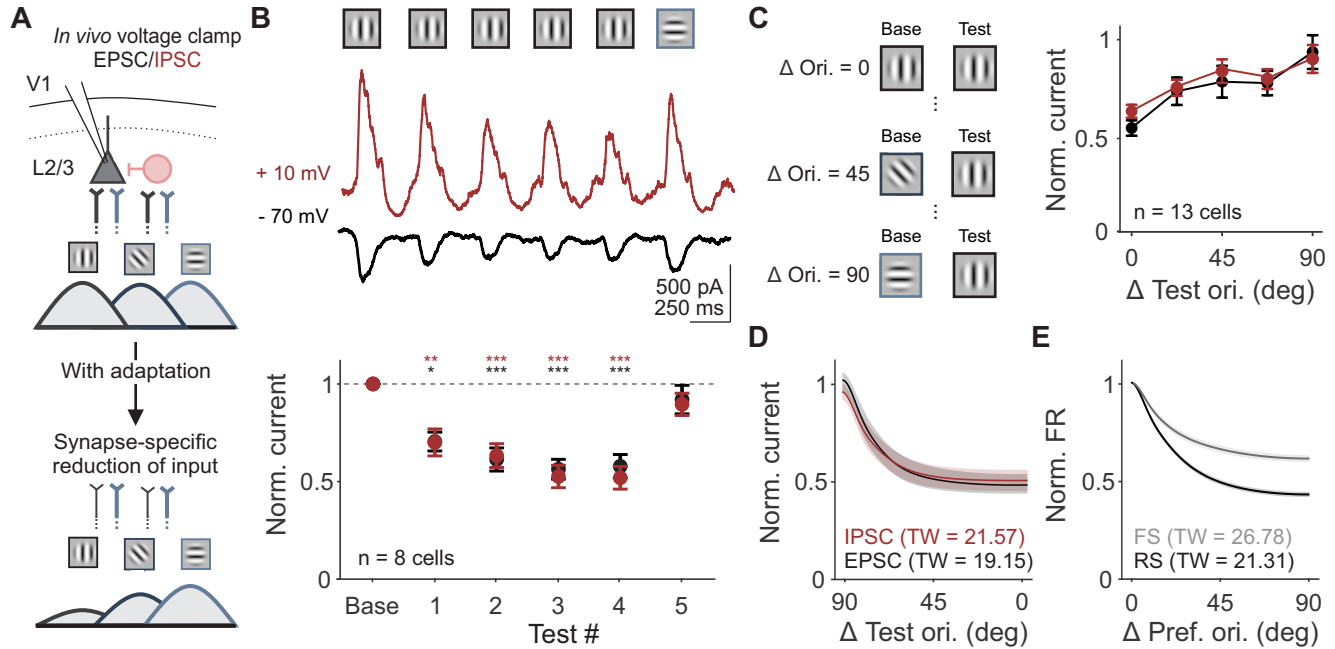


**Figure 3. Changes in synaptic input are selective to previously activated synapses. A.** Schematic of proposed model of synapse-specific effect of adaptation on excitatory inputs from L4 to L2/3. This generates orientation-selective decrease of synaptic inputs to both excitatory and inhibitory L2/3 neurons. Color of axons correspond to L4 inputs to L2/3 synapses tuned to vertical (black) versus horizontal (blue) orientations. Line thickness represents strength of inputs. **B.** Top: Visual stimulus paradigm with repeated presentation of the same stimulus orientation (baseline and test 1-4) followed by an orthogonal orientation (test 5). Middle: Average stimulus evoked EPSCs (black) and IPSCs (red) for an example cell. Bottom: Average normalized current (test/baseline) for all cells (n = 8). Response to the orthogonal orientation is normalized to its own baseline. Error bar is SEM across cells. **C.** Left: Schematic of stimuli presented to measure the tuning width of adaptation. Test orientation was kept constant while the baseline orientation varied. Right: Average normalized current (test/baseline, where the baseline is the same orientation as the test) as a function of similarity between baseline and test stimuli for EPSCs and IPSCs for all cells (n = 13). **D.** Average adaptation tuning curve fits from data in **C**. Shaded error is SEM across cells. Tuning width (TW) is half-width at half-max. **E.** Average orientation tuning curve fits from extracellular recording of V1 RS (black) and FS (gray) units.

## Figure 4
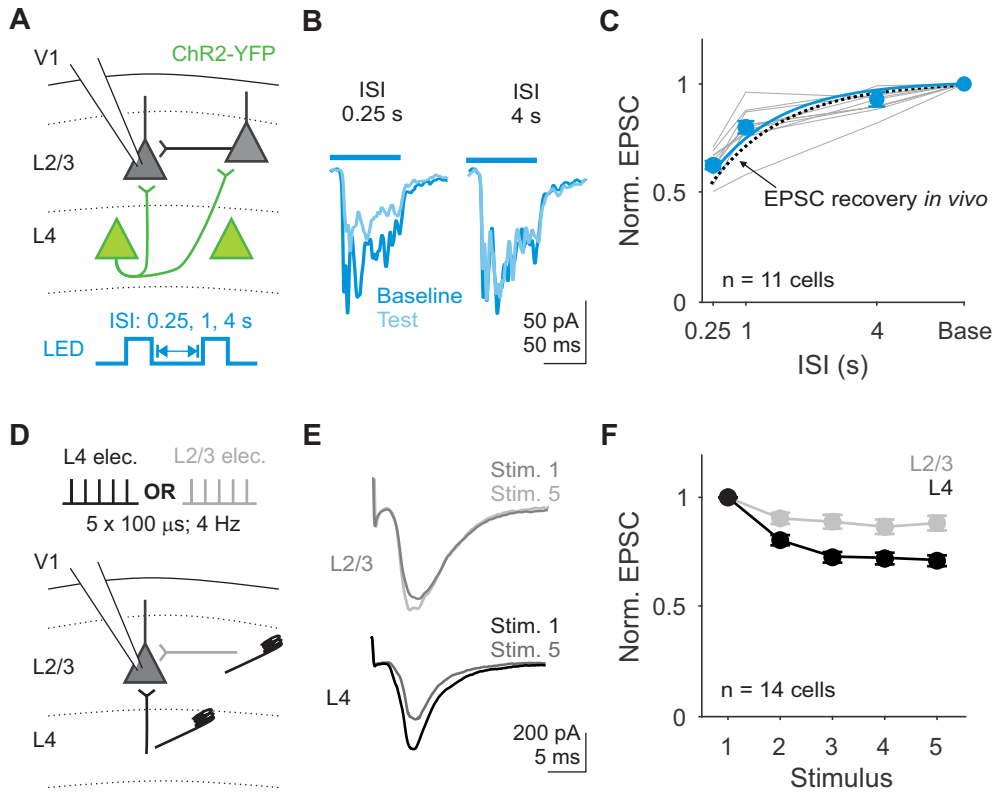


**Figure 4. Excitatory inputs to L2/3 neurons decrease with repeated stimulation *in vitro*. A.** Schematic of setup for recording EPSCs in L2/3 neurons during optogenetic stimulation of L4. Two 0.1 s square pulses of blue light (baseline and test) were used to activate L4 neurons. **B.** Average traces during baseline (dark blue) and test (light blue) stimuli from an example cell during 0.25 s (left) versus 4 s (right) ISI trials. **C.** Average normalized EPSC amplitudes (test/baseline) as a function of ISI for each cell (gray) and the across all cells (blue). Blue line is exponential fit to the average across cells. Dashed line is exponential fit from EPSCs recorded *in vivo* in **Figure 2**. Error bar is SEM across cells (n = 11). **D.** Schematic for recording EPSCs from a L2/3 pyramidal cell while electrically stimulating L4 or L2/3 inputs on alternating trials. **E.** Average EPSCs from an example cell in response to stimulation of L2/3 (top; gray) or L4 (bottom; black). **F.** Average EPSC amplitudes normalized to the first stimulus in response to L2/3 (gray) and L4 (black) stimulation. Error bar is SEM across cells.

## Figure 5
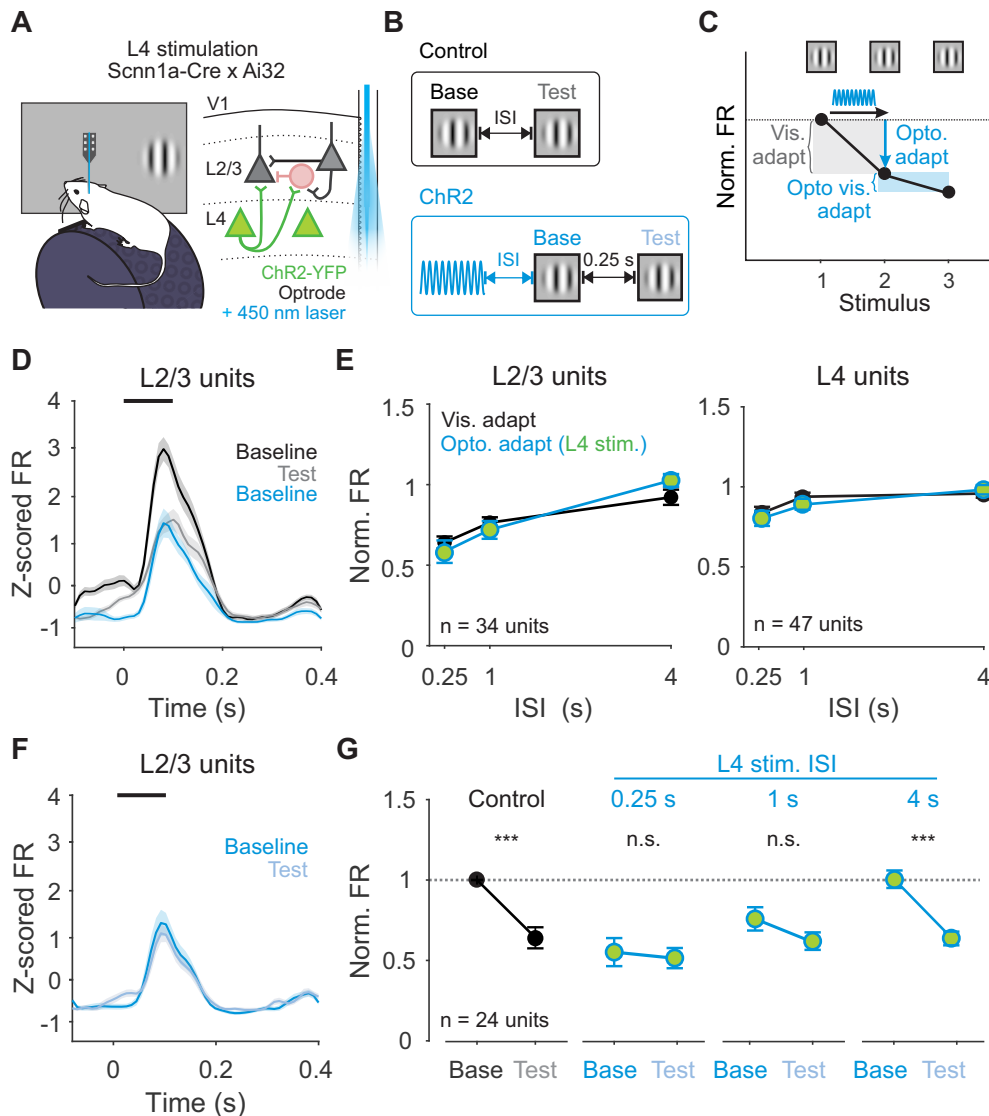


**Figure 5. Activation of L4 neurons is sufficient to recapitulate the effects of visual adaptation. A.** Schematic of in vivo extracellular recording setup with optrode coupled to a 450 nm laser. **B.** Structure of control trials (black) and ChR2 activation trials (blue). On control trials, baseline and test stimuli are presented with varying ISI. On ChR2 activation trials, 0.5 s of sinusoidal blue light is used to activate L4 neurons optogenetically at varying intervals prior to baseline visual stimulus presentation. **C.** Visual adaptation is quantified as the response to the test divided by the response to the baseline stimulus (gray shaded box). Optogenetic adaptation is quantified as the response to the baseline stimulus in ChR2 activation trials divided by the response to the baseline stimulus in control trials (blue arrow). Optogenetic visual adaptation is quantified as the response to the test stimulus divided by the baseline stimulus following on ChR2 activation trials (blue shaded box). **D.** Average z-scored PSTH for L2/3 units during baseline (black) and test (gray) stimuli in control trials and baseline stimulus in ChR2 activation trials (blue; n = 34 units). Black line indicates stimulus presentation. Shaded error is SEM across unit. **E.** Comparison of visual adaptation (black) and optogenetic adaptation (blue) in L2/3 (left) and L4 (right) units. Green fill indicates optogenetic stimulation of L4. **F.** Average z-scored PSTH for L2/3 units during baseline (blue) and test (light blue) stimuli in L4 ChR2 activation trials. **G.** Visual adaptation (black) and Optogenetic visual adaptation (blue) with 0.25 s ISI at increasing intervals after L4 stimulation (0.25 s, 1 s, 4 s). Normalized firing rate is calculated relative to baseline visual response in control trials (horizontal dashed line). Error bar is SEM across units.
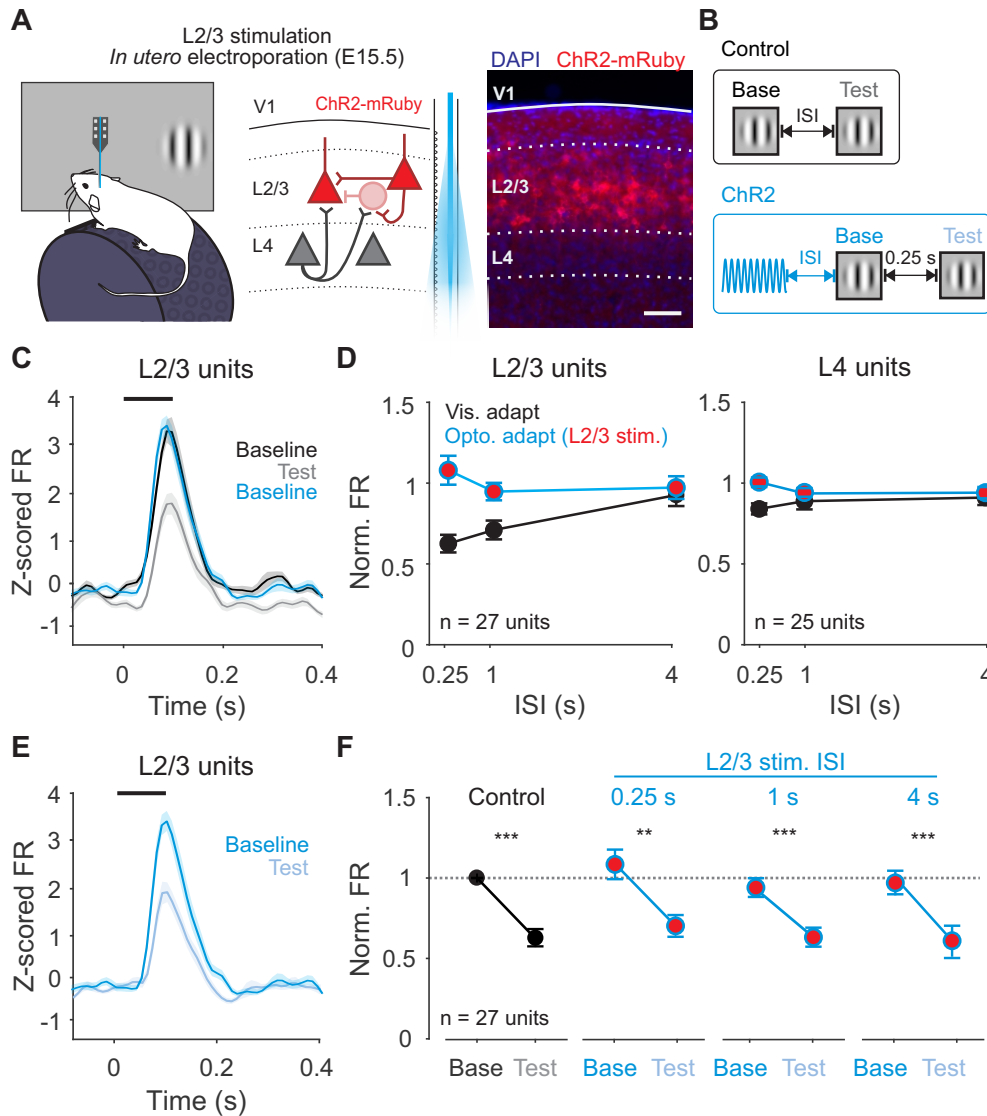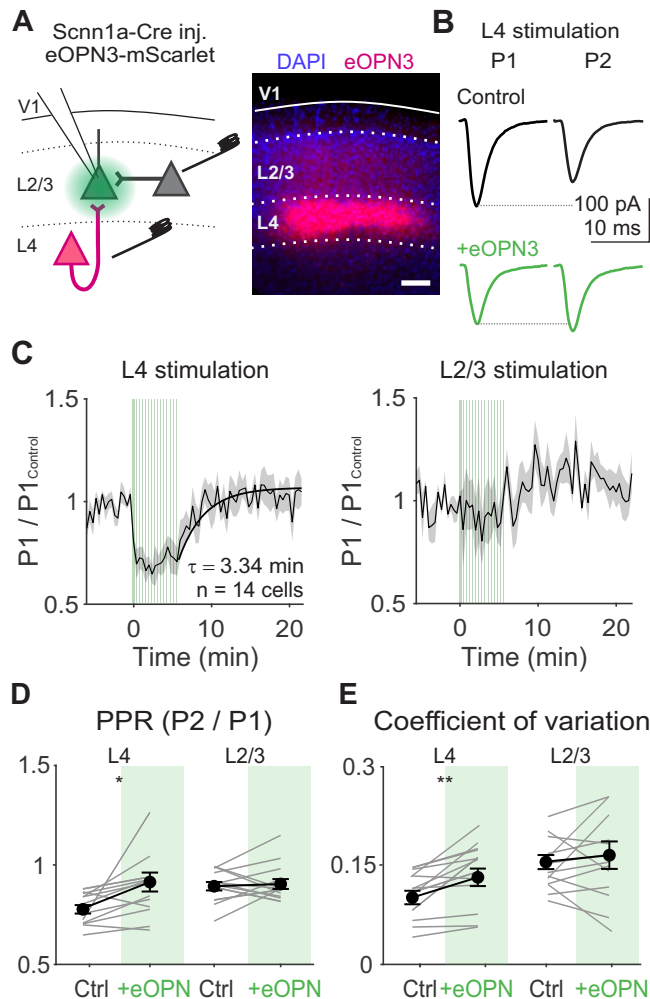
# Figure 6



**Figure 6. Activation of L2/3 neurons does not recapitulate the effects of visual adaptation. A.** Left: Schematic of in vivo extracellular recording setup in mice expressing ChR2 in L2/3 neurons. Right: expression of ChR2-mRuby in L2/3 neurons following in utero electroporation. Scale bar is 100 μm. **B.** Structure of control trials (black) and ChR2 activation trials (blue). **C.** Average z-scored PSTH for L2/3 units during baseline (black) and test (gray) stimuli in control trials and baseline stimulus in ChR2 activation trials (blue; n = 27 units). Black line indicates stimulus presentation. Shaded error is SEM across units. **D.** Comparison of visual adaptation (black) and optogenetic adaptation (blue) in L2/3 (left) and L4 (right) units. Red fill indicates optogenetic stimulation of L2/3. **E.** Average z-scored PSTH for L2/3 units during baseline (blue) and test (light blue) stimuli in L2/3 ChR2 activation trials. **F.** Visual adaptation (black) and Optogenetic visual adaptation (blue) with 0.25 s ISI at increasing intervals after L2/3 stimulation (0.25 s, 1 s, 4 s). Normalized firing rate is calculated relative to baseline visual response in control trials (horizontal dashed line). Error bar is SEM across units.

## Figure 7



**Figure 7. Activation of eOPN3 in L4 terminals reduces probability of release at inputs onto L2/3 neurons. A.** Left: Schematic of *in vitro* recording setup for recording EPSCs in L2/3 neurons while electrically stimulating L4 or L2/3. eOPN3 expressed in L4 neurons is activated with green light over L4 terminals in L2/3. Right: Example image of viral expression pattern. Scale bar is 100 μm. **B.** EPSCs from an example cell in response to L4 stimulation during first (P1) and second (P2) stimuli in a train (4 Hz), either before (black) or after eOPN3 activation (green). **C.** Average time course of normalized P1 EPSC amplitudes following L4 (left) or L2/3 (right) stimulation aligned to the time of eOPN3 activation (n = 14 cells). Vertical green lines indicate eOPN3 activation trials: induction of 10 s of pulsed green light prior to visual stimulus presentation, followed by a top-up of 0.5 s of pulsed green light prior. Black curve is exponential fit to recovery. Shaded error is SEM across cells. **D.** Paired pulse ratio (PPR) during L4 or L2/3 stimulation for individual cells (gray lines) and the average of all cells (black) in control (white) and after eOPN activation (green). Error bar is SEM across cells. **E.** Same as **D**, for coefficient of variation.
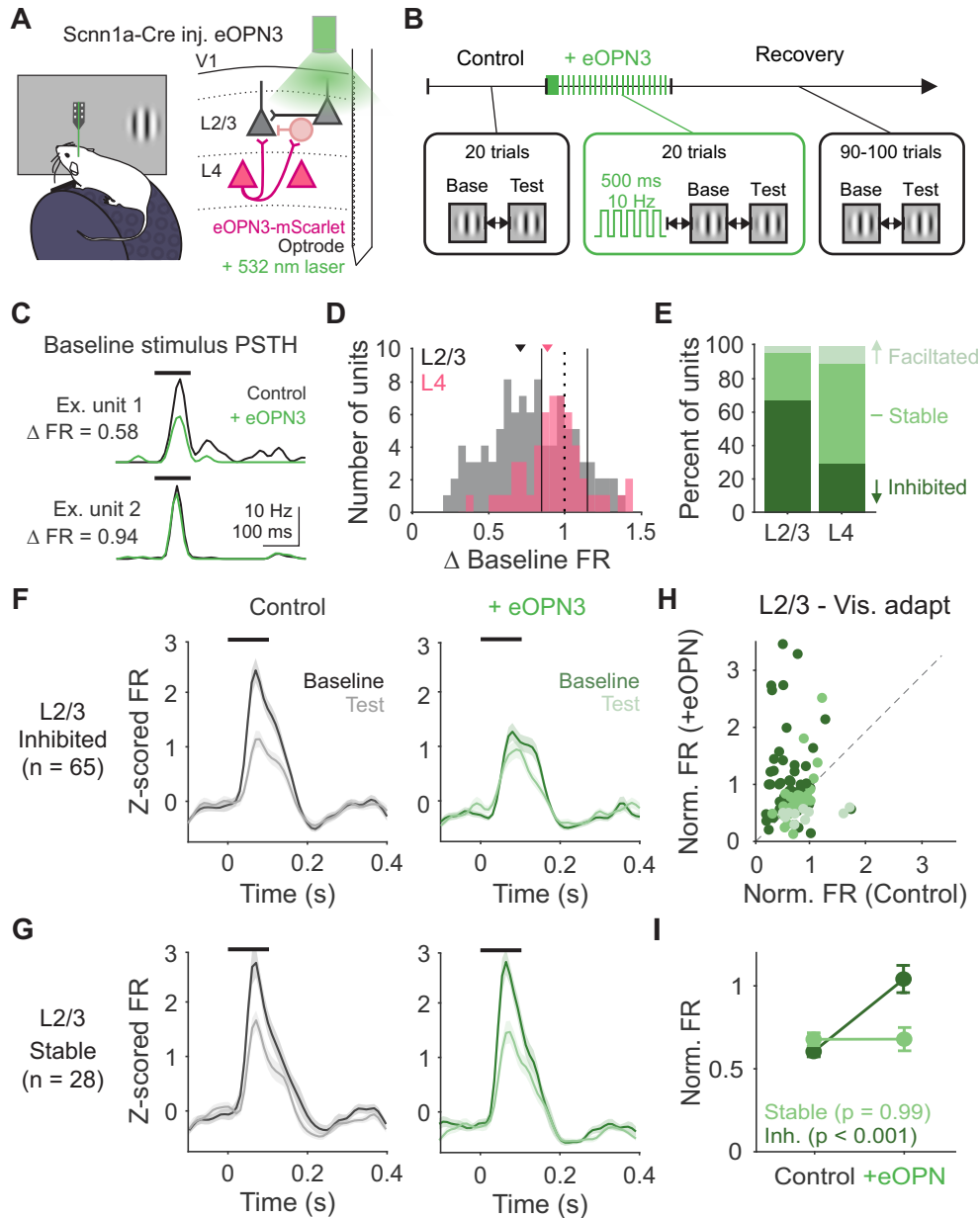
## Figure 8



**Figure 8. Decreasing probability of release at L4 terminals decreases visual adaptation *in vivo*. A.** Schematic of recording setup and eOPN3 expression with green light illumination outside of the brain. **B.** Block-wise trial structure for measuring effects of eOPN3 activation on visual adaptation. Visual stimuli are always presented with 0.25 s ISI. eOPN3 activation block consist of an induction of 10 s of pulsed green light prior at the start of the block, followed by a top-up of 0.5 s of pulsed green light prior to visual stimulus presentation on each trial. **C.** PSTHs for two example units in control (black) and eOPN3 activation (green) trials. Δ FR is calculated as the change in peak stimulus-evoked response. **D.** Distribution of change in visually-evoked responses to the baseline stimulus in L4 (pink; n = 61) and L2/3 (gray; n = 105) units. Vertical solid lines indicate thresholds for categorization as inhibited (< 0.8), stable (> 0.8 and < 1.2), or facilitated (> 1.2). **E.** Percent of units categorized as inhibited, stable, or facilitated in L2/3 and L4. **F.** Average z-scored PSTH of inhibited L2/3 units (n = 65) in response to baseline (dark) and test (light) stimuli during control trials (left, black) and during eOPN3 activation trials (right, green). Black line indicates stimulus presentation. Shaded error is SEM across units. **G.** Same as **F**, for stable L2/3 units (n = 28). **H.** Comparison of normalized response (test/baseline) in control and eOPN3 activation trials, for all L2/3 units colored by categorization in **E. I.** Average normalized response for inhibited (dark green) and stable (light green) units in L2/3. Error bar is SEM across units.
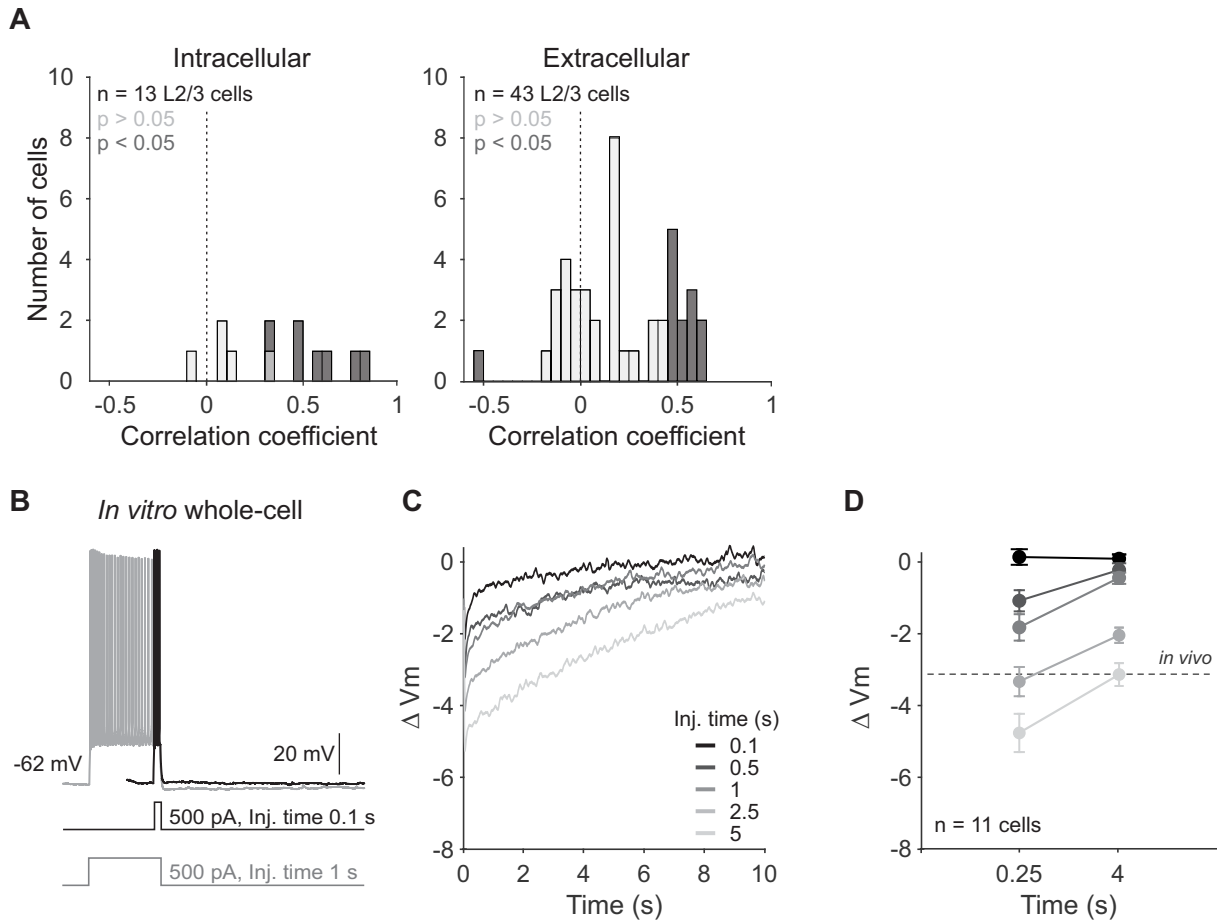
**Figure S1. Rapid adaptation does not induce cell-intrinsic fatigue, related to Figure 1. A.** Histogram of single trial correlation of spikes elicited in response to baseline and test stimuli for 0.25 ISI condition from intracellular (left; n = 13 cells) and extracellular (right; n = 43 units) L2/3 *in vivo* recordings. Dark gray bars indicate significant correlations. **B.** Current clamp recording in example L2/3 pyramidal cell in response to current injections of two durations (black = 0.1 s, gray = 1 s). **C.** Change in membrane potential (Vm) following offset of increasing current injection durations in the example cell in **B**. **D.** Average change in membrane potential after current injection offset at recovery times when spike output is suppressed (0.25 s) or recovered (4 s) *in vivo* for increasing current durations. Dashed line is average change in stimulus-evoked membrane potential *in vivo*. Error bar is SEM across cells
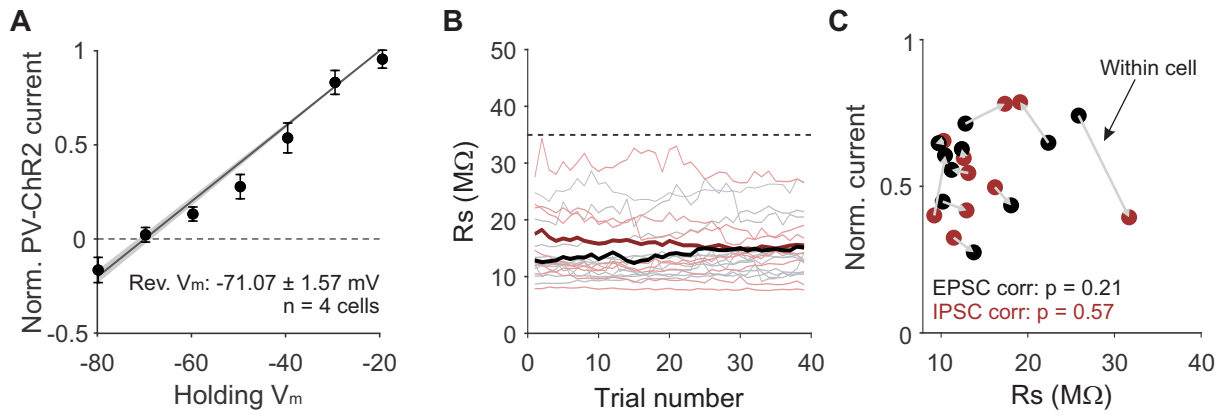
**Figure S2. Whole-cell voltage clamp recording of EPSCs and IPSCs *in vivo*, related to Figure 2.**
**A.** Reversal potential of currents evoked with optogenetic activation of parvalbumin-expressing (PV) interneurons expressing Channelrhodopsin-2 (ChR2) to calibrate reversal potential for inhibitory currents in vivo (PV-Cre mice injected with AAV2/1.hSyn.ChR2-YFP; n = 4 cells). **B.** Series resistance (Rs) during recording of EPSCs (black) and IPSCs (red). Thick lines are average across cells. Dashed line is cutoff used for series resistance inclusion criteria. **C.** Normalized current (baseline/test; 0.25 s ISI) as a function of series resistance for all recordings. Grey arrows connect currents recorded within the same cell and direction reflects the order of recording. P-value is significance of Pearson correlation.
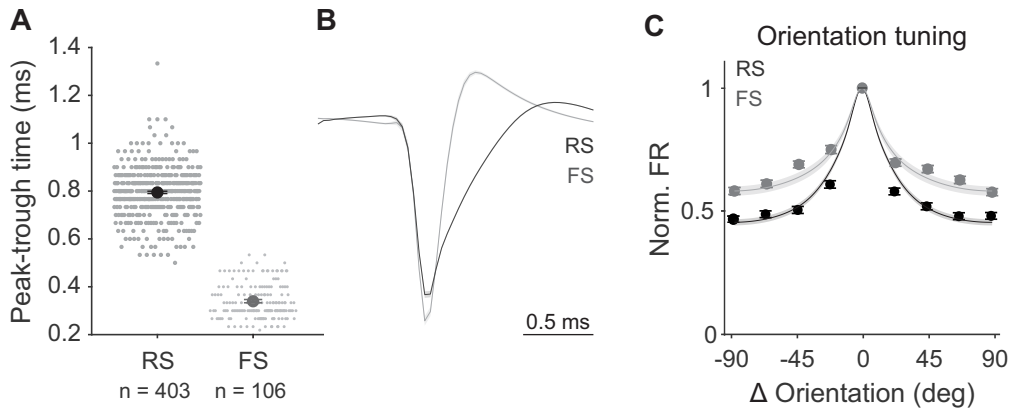
**Figure S3. Separation of FS and RS units and comparison of orientation tuning, related to Figures 2 and 3. A.** Peak-trough time of spike waveforms from units classified as regular spiking (RS, black) or fast spiking (FS, grey). **B.** Average spike waveforms from the units in **A**. Shaded error is SEM across units. **C.** Average orientation tuning curves aligned to preferred orientation for each unit. Points are averaged normalized response across units. Curves are averages of the von Mises fit for individual units.
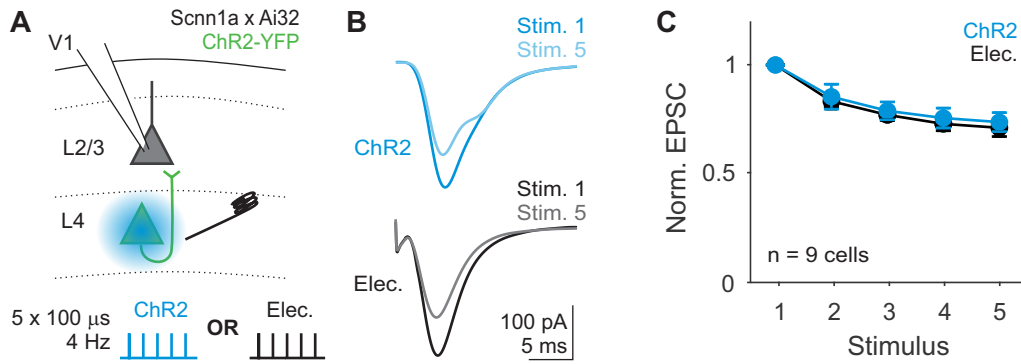
**Figure S4. EPSCs in L2/3 measured with ChR2 and electrical stimulation, related to Figure 4. A.** Schematic of recording EPSCs from a L2/3 pyramidal cell while stimulating L4 neurons optogenetically or electrically on alternating trials. **B.** Average EPSCs from an example cell in response to optogenetic (blue) or electrical (black) stimulation of L4 for the first (dark) and last (light) stimulus in the train. **C.** Average EPSC amplitude normalized to first pulse within stimulation type. Error bar is SEM across cells. Two-way ANOVA, p = 0.51 for effect of stimulation type.
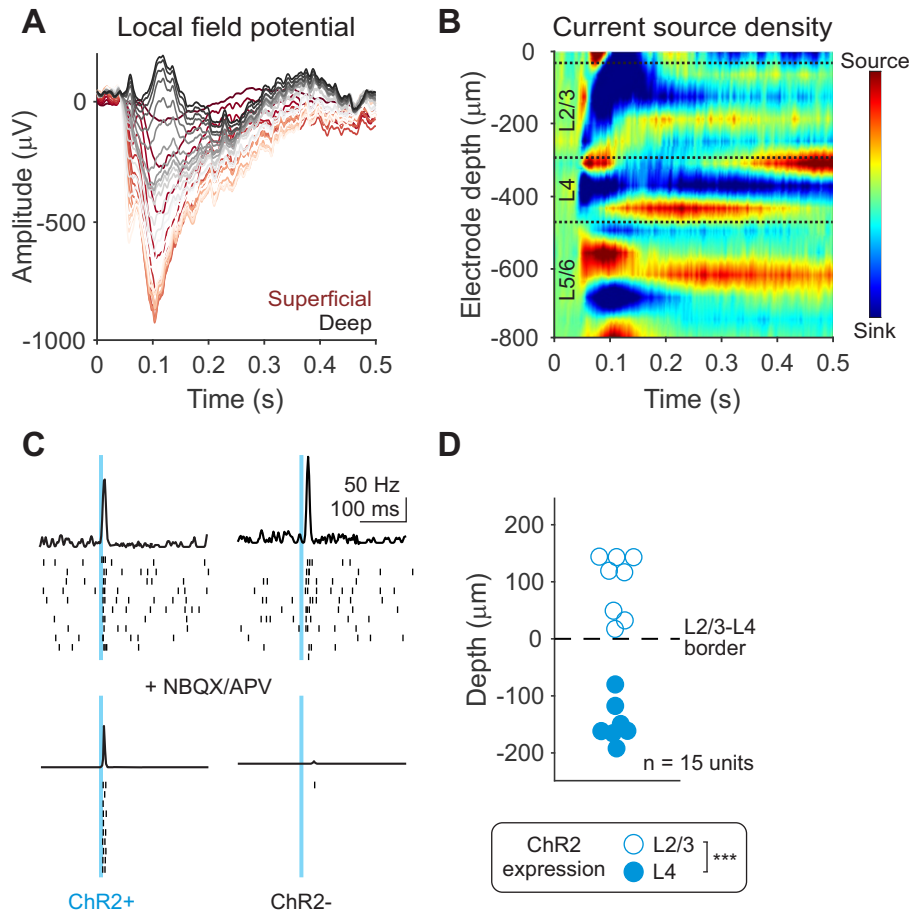
**Figure S5. Identification of layer boundaries for classifying units as L2/3 or L4, related to Figures 5, 6 and 8. A.** Local field potential (LFP) measured across cortical depths during a drifting grating stimulus from an example recording. Traces are colored according to contact site from superficial (red) to deep (black). **B.** Current source density (CSD) calculated using the LFP in **A**. Dashed lines indicate layer boundaries assigned based on this map. L4 was assigned by identifying an early onset sink and L2/3 was identified as the later onset sink above it. **C.** Example units identified as ChR2+ (left) or ChR2- (right). PSTH and spike rasters in response to blue laser pulses (10 ms) before (top) and after (bottom) pharmacological block of excitatory transmission (**STAR Methods**). **D.** Depth of ChR2-expressing units relative to L2/3-L4 boundary identified using the CSD. Marker fill indicates ChR2 expression layer (unfilled = L2/3, in utero electroporated mice; filled = L4, Scnn1a x Ai32 mice; depth of L2/3 vs L4 expression: p < 0.001, un-paired t-test).
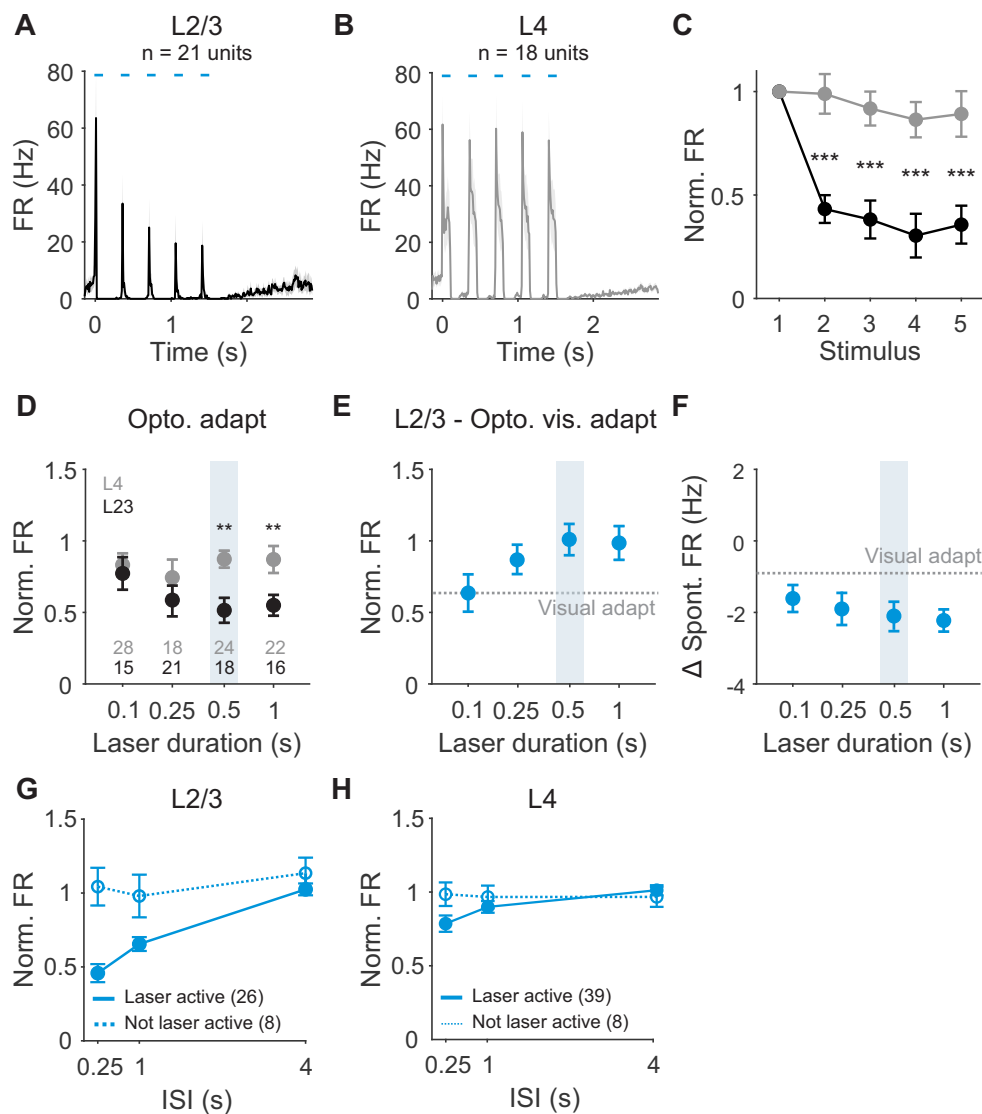
**Figure S6. Effects of optogenetic activation of L4 neurons, related to Figure 5. A.** Average PSTH of laser active L2/3 units during optogenetic activation of L4 neurons with 5, 0.1 s square pulses of blue light. **B.** Same as **A**, for L4 units. **C.** Peak firing rate for each stimulus pulse, normalized to the first pulse in the train for L2/3 (black) and L4 (grey) units. Error bar is SEM across units. L2/3 $p < 0.001$ for stimulus 2-5 vs 1, one-way ANOVA with post hoc Tukey test. **D.** Optogenetic adaptation measured in L2/3 and L4 units across different laser durations (L4 vs L2/3, 0.5 s laser duration: $p = 0.006$; 1 s laser duration: $p = 0.009$, unpaired t-tests). Shaded box indicates laser duration used for main figure experiments. **E.** Visual adaptation measured in L2/3 neurons following different durations of optogenetic activation of L4 neurons. Dashed line is visual adaptation in the absence of L4 stimulation. **F.** Change in spontaneous firing rate after different durations of L4 activation. Dashed line is spontaneous firing rate after visual adaptation. **G.** L2/3 optogenetic adaptation in units divided by units that were significantly modulated by L4 ChR2 stimulation (solid line) or not (dashed line). **H.** Same as **G**, for L4 units.
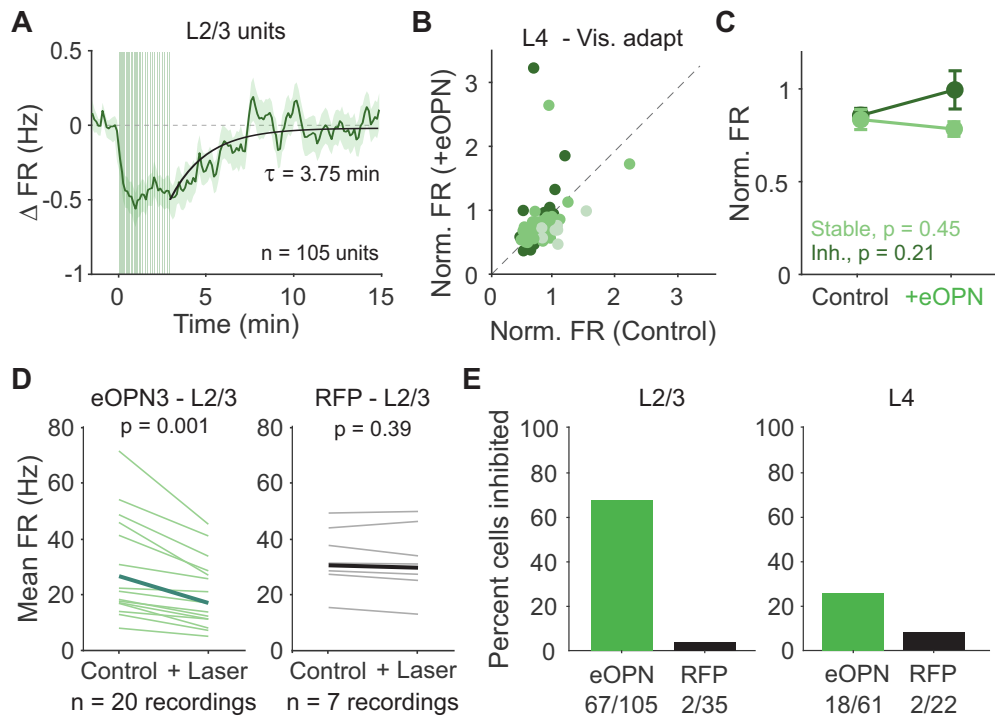
**Figure S7. Green laser alone does not affect firing rates, related to Figure 8. A.** Average time course of stimulus-evoked, z-scored firing rate aligned to eOPN3 activation for all units recorded in L2/3 (n = 105). Green vertical lines indicate eOPN3 activation trials. Black curve is fit to the recovery from eOPN3 activation. Shaded error is SEM across units. **B.** Comparison of normalized response (test/baseline) in control and eOPN3 activation trials, for all L4 units colored by categorization in **Figure 8E** (dark green = inhibited, medium green = stable, light green = facilitated). **C.** Average normalized response for inhibited (dark green) and stable (light green) units in L4. Error bar is SEM across units. **D.** Average visually-evoked firing rate of L2/3 neurons during control and laser stimulation trials in eOPN3 (left, green) or RFP control (right, black) recordings. Individual lines are average response of all L2/3 neurons in each session, thick line is mean across sessions (eOPN: paired t-test, p < 0.001; RFP: paired t-test p = 0.39). **E.** Left: Fraction of L2/3 units classified as inhibited from recordings with eOPN3 (green) or RFP control (black) in L4 neurons. Right: Same as left, for L4 units.
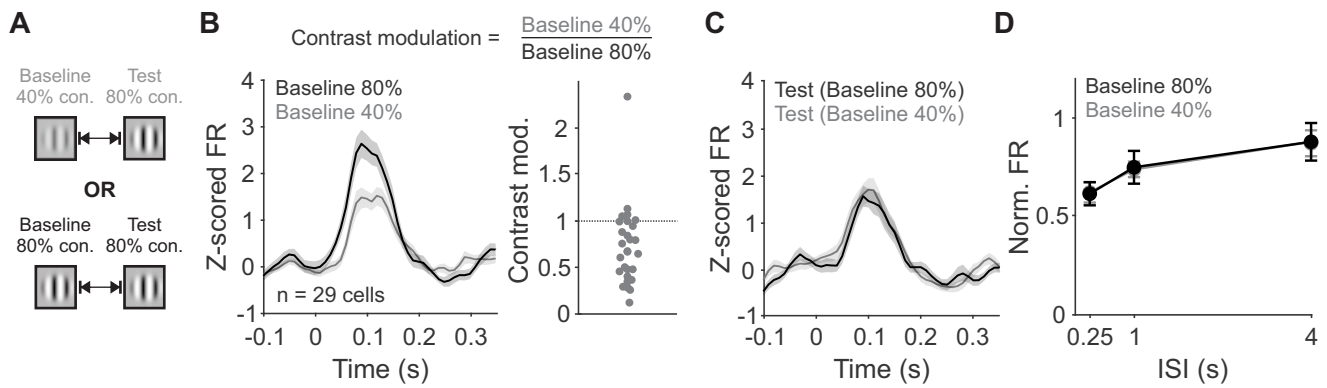
**Figure S8. Effect of low contrast baseline stimulus on adaptation in L2/3, related to Figure 8. A.** Schematic of visual stimulus. Baseline stimulus was either low (40%) or high (80%) contrast and test stimulus was always high contrast. **B.** Left: Z-scored PSTH of L2/3 units during high contrast (black) or low contrast (gray) baseline visual stimulus presentation. Right: Fractional change in peak firing rate during baseline stimulus for high versus low contrast. **C.** Z-scored PSTH during test visual stimulus presentation with baseline high (black) or low contrast (gray). **D.** Average normalized firing rate (test/baseline) with high or low contrast baseline stimulus. Test responses for both trial types was divided by the baseline response to high contrast (two-way ANOVA, effect of contrast, p = 0.45).